Aalto University
School of Science

Aaro Järvinen

Simulations of Tungsten Transport in the Edge of JET ELMy H-mode Plasmas

Master's thesis submitted in partial fulfillment of the requirements for the degree of Master of Science in Technology in the Degree Programme in Engineering Physics and Mathematics.

Espoo, 22.4.2012

Supervisor: Professor Rainer Salomaa

Instructor: PhD Mathias Groth

Aalto-yliopisto Perustieteiden korkeakoulu	DIPLOMITYÖN TIIVISTELMÄ
Tekijä: Aaro Järvinen	
Työn nimi: Volframin kulkeutumisen simulointia JETin ELMisen korkean koossapidon plasman reunalla	
Title in English: Simulations of Tungsten Transport in the Edge of JET ELMy H-mode Plasmas	
Tutkinto-ohjelma: Teknillisen fysiikan ja matematiikan tutkinto-ohjelma	
Pääaine: Energiatieteet	Sivuaine: Matematiikka
Opetusyksikön (ent. professuuri) koodi: Tfy-56	
Työn valvoja: Professori Rainer Salomaa	Työn ohjaaja(t): PhD Mathias Groth

Tiivistelmä:

ITER koereaktorin ydinfuusio-ohjelman aikana tullaan todennäköisesti käyttämään volframisia komponentteja diverttorin alueella, koska volframi kaappaa vain vähän polttoainetta eikä muodosta seinälle kertyviä yhdisteitä polttoaineen kanssa. Vaikka volframi kestää hyvin deuteriumin aiheuttamaa eroosiota, volframin eroosio plasman epäpuhtauksien ja reunamoodien (ELM) vaikutuksesta voi johtaa merkittävään komponenttien kulumiseen, korkeaan volframipitoisuuteen plasmassa, voimakkaaseen keskustan säteilyyn ja plasman tehon heikkenemiseen. ITER koereaktorin ensiseinän materiaalien aiheuttamien kysymysten takia, JET-tokamakin ensiseinä on vaihdettu ITER-tyyppiseksi, joka koostuu beryllium rajoittimista ja volframista valmistetuista diverttorilevyistä. Tässä työssä tutkitaan plasman keskustan volframisaastumista yhdessä JET-tokamakin ITER-tyyppisen ensiseinän referenssiplasmassa. Volframin eroosiota ja kulkeutumista mallinnetaan kvasi-kineettisellä Monte-Carlo ohjelmalla DIVIMP käyttäen taustaplasmoja, joiden dynaaminen aikakehitys on laskettu 2-D fluidiohjelmalla EDGE2D/EIRENE. EDGE2D/EIRENE-simulaatiot on säädetty vastaamaan ELMien välisiä mittauksia ulkokeskilinjan Thomsonin sironta, sekä diverttorilevyjen Langmuir sondi ja infrapuna kamera diagnostiikoilla. Lisäksi ELMin suuruus, sekä ELMin virtaavan ja johtuvan osuuden suhde on asetettu vastaamaan mittaustuloksia tekijän 2 virhemarginaalilla. ELMejä mallinnetaan tässä työssä *ad hoc* -menetelmällä kasvattamalla lyhyeksi ajaksi plasman kentän poikkisuuntaista diffuusiota ulkoisen keskilinjan ympäristössä. Saatuja ELM ratkaisuja käytetään DIVIMP simulaatioissa, joissa mallinnetaan volframin eroosion ja keskustaan vuotamisen aikariippuvuutta. Volframin eroosiota laskettaessa on otettu huomioon deuteriumin, sekä kevyiden plasman epäpuhtauksien vaikutus. ELM johtaa EDGE2D/EIRENE-simulaatioissa kalvorajoitettuun plasmaan, jossa diverttorilevyjen plasmalämpötilat ovat muutaman 100 eV:n luokkaa. Kalvorajoitettu korkean levylämpötilan plasma johtaa merkittävään volframin eroosioon ja keskustaan kulkeutumiseen. Levylämpötilat pysyvät suurina ensimmäisten muutaman 100 μs aikana ELMin jälkeen. Plasman tiheys diverttorilevyjen edessä alkaa nousta noin 1 millisekunnin jälkeen, mikä johtaa korkean neutraalikierrätyksen plasmaan laskien lämpötilan diverttorilevyjen edessä nopeasti muutamaan 10 eV:in. Korkean neutraalikierrätyksen alkaessa, volframin eroosio ja keskustaan kulkeutuminen heikkenevät voimakkaasti. ELMit johtavat siis voimakkaaseen hetkelliseen plasman saastumiseen, joka määrää suurelta osin plasman keskimääräisen volframikonsentraation. Plasman volframisaastuminen osoittautuu siis tasapainoprosessiksi, jossa ELMien aiheuttama keskustan saastuminen ja puhdistuminen kilpailevat keskenään. Volframisaastuminen ELMisessä H-moodi plasmassa määräytyy siis suurelta osin ELMien ominaisuuksien perusteella. Tässä työssä volframikonsentraatiolle saatiin arvio $10^{-6} - 10^{-5}$. Noin 50% keskustaplasman volframisaastumisesta johtui deuteriumin ELMin aikana aiheuttamasta eroosiosta. Itseräiskymisen huomioonottaminen johtaa voimakkaaseen volframin eroosion kasvamiseen ELMin aikana. Täten itseräiskyminen johtanee saatuja arvioita suurempaan volframikonsentraatioon.

Päivämäärä: 22.4.2012	Kieli: Englanti	Sivumäärä: 69
Avainsanat: DIVIMP, EDGE2D, EIRENE, ELM, ILW, PSI, Tungsten		

Aalto University School of Science	ABSTRACT OF THE MASTER'S THESIS

Author: Aaro Järvinen

Title: Simulations of Tungsten Transport in the Edge of JET ELMy H-mode Plasmas

Title in Finnish: Volframin kulkeutumisen simulointia JETin ELMisen korkean koossapidon plasman reunalla

Degree Programme: Degree Programme in Engineering Physics and Mathematics

Major subject: Advanced Energy Systems	Minor subject: Mathematics

Chair (code): Tfy-56

Supervisor: Professor Rainer Salomaa	Instructor: PhD Mathias Groth

Abstract:

Tungsten plasma-facing components (PFCs) are foreseen in the divertor of ITER during the activated operational phase due to low fuel retention in the bulk material and the absence of co-deposition. While physical sputtering of deuterium is suppressed in semi-detached plasma conditions, tungsten sputtering by deuterium during edge localized modes (ELMs) and by plasma impurities may lead to significant tungsten erosion, high tungsten concentrations in the core plasma exceeding 10^{-5}, strong radiation and, therefore, to reduction of plasma performance. Understanding the time-evolution of tungsten erosion and transport in ELMy H-mode plasmas is, thus, essential for optimising tungsten impurity screening in tokamaks operating with tungsten PFCs. To address the issues related to tungsten sources and transport in ITER, an ITER-like wall has been installed in the JET tokamak with tungsten divertor PFCs and bulk beryllium main chamber limiters. In this study, tungsten contamination is simulated for one of the JET ITER-like wall reference plasmas of high triangularity. Tungsten erosion and transport are simulated with the quasi-kinetic Monte Carlo trace-ion code DIVIMP on background plasmas dynamically evolved in time with the 2-D multi-fluid code EDGE2D/EIRENE. The EDGE2D/EIRENE simulations are adjusted to match the pre-ELM outer mid-plane (OMP) Thomson scattering, target Langmuir probe and target infra-red camera measurements, as well as to reproduce within a factor of two the total ELM magnitude and the ratio of the convective ELM losses to the conductive ones. ELMs are simulated *ad hoc* by imposing short duration enhancements for the cross-field diffusion coefficients around the OMP. DIVIMP is executed on the obtained ELM background plasma solutions to model the time-evolution of tungsten erosion and core leakage. Tungsten erosion due to background deuterium and small percentages of light impurities, such as neon, nitrogen and beryllium, are taken into account. The ELM onset in EDGE2D/EIRENE is characterized by sheath-limited ($v_e^* \sim 2$) SOL plasma conditions with target temperatures of the order of a few 100 eV. The sheath-limited, high target temperature conditions lead to a significant increase of tungsten sputtering and divertor leakage. The target temperatures remain elevated during the first few 100 μs of the ELM event. The target densities begin to increase roughly 1 millisecond after the ELM onset, which leads to high recycling target conditions and lowers the target temperatures rapidly to the range of a few 10 eV. Consequently, tungsten sputtering and divertor leakage are considerably suppressed. Accordingly, ELMs impose a strong temporal increase of the core tungsten contamination, which dominantly determines the amount of tungsten in the core. Therefore, the core tungsten contamination of ELMy H-mode plasmas becomes a balance process between the ELM induced core purging, and the ELM caused core contamination, thus being ultimately determined by the ELM characteristics. An estimated tungsten core concentration of $10^{-6} - 10^{-5}$ was obtained. Roughly 50% of the core contamination originated from sputtering due to deuterium impact during ELMs. Including self-sputtering leads to a short duration tungsten run-away process during the intra-ELM phase. Therefore, the self-sputtering presumably increases the core contamination above the values obtained in this study.

Date: 22.4.2012	Language: English	Number of pages: 69

Keywords: DIVIMP, EDGE2D, EIRENE, ELM, ILW, PSI, Tungsten

Preface

This thesis required a substantial amount of work and hours of frustration. The process would not have been possible without the contributions of several people. First and foremost, I would like to thank my mentor Mathias Groth, who has patiently introduced and explained the essence of the SOL plasma physics to me in the course of the last two years. I am also grateful to Sven Wiesen who gave me the possibility to contribute to his EPS 2011 work by simulating tungsten erosion and transport with DIVIMP for his ELM simulations done with the integrated code suite JINTRAC. This thesis got its stimulus from that project. Karl Krieger and Toni Makkonen are acknowledged for guiding me through my first steps with the simulation code DIVIMP. I would like to thank Carine Giroud for requesting simulations of tungsten contamination, thus offering this topic for me to work on. I am thankful for the help of Jim Strachan, Gerard Corrigan, Paula Belo, and David Moulton in their insight for the numerical and physical properties of EDGE2D/EIRENE. I would like to thank Thomas Eich for helping me to understand the experimental side of the ELM scrape-off layer energy transport. Discussions with David Tskhakaya and Eva Havlickova during the last modelling meeting at JET in March 2012 were critical for me in understanding the limitations of fluid simulations for addressing ELM transport physics. I would like to acknowledge the work done by diagnosticians: Stefan Jachmich for the inter-ELM Langmuir probe measurements, Thomas Eich for the target infra-red measurements, Marc Beurskens for the outer mid-plane Thomson scattering profiles, and Michael Lehnen for the bolometry data. Furthermore, I would like to thank Rainer Salomaa, Taina Kurki-Suonio, and Mathias Groth for offering me the possibility to do research in the field of applied plasma physics. In addition, I would like thank all the others, who have participated in this work, but are not listed here due to the vast amount of contributors. Finally, I would like to thank my family and friends who have put up with me while I have devoted most of my time on this thesis during the last couple of months. This would not have been possible without you!

Contents

Introduction

Since the late 18th century, mankind has exploited fossil fuels, such as coal, oil and natural gas, as an economic energy source for increasing the standard of living. Still, in the 21st century, the ever-growing economy, as well as rapid industrialization of developing countries, will continue to demand more and more energy. The fossil fuel supplies, which have met most of this increasing demand so far, are, however, very limited. They are foreseen to run out within the following centuries [1], thus jeopardizing the basis of the modern society. In addition, burning fossil fuels produce high amounts of green house gases, the emission of which must be reduced to restrict the global warming within the acceptable level of 2 degrees compared to the pre-industrial era [2]. Therefore, alternative energy sources with acceptable costs of economic and natural resources must be developed to overcome the otherwise inevitable energy and climate crisis within the next centuries.

Nuclear fusion, the process taking place in stars, offers that desirable energy source. Not only does it provide practically unlimited fuel resources, but also it does not cause any significant pollution. Green house gases are not produced in the fusion reaction, and the slight activation of the reactor components is negligible compared to the radioactive inventory produced by the traditional nuclear fission power plants. Until fusion power plants become commercially available, fission power plants are, nevertheless, considered as a viable fossil-fuel-alternative energy source to reduce greenhouse gas emissions.

The technology required for a nuclear fusion reactor is, however, very advanced. *Tokamaks* are currently the leading fusion reactor concept due to their high fusion performance. In a tokamak, the fuel is heated up to 150 million Kelvins and, thus, brought into a plasma state and confined with strong magnetic fields. Despite this, the *plasma-surface interaction* (PSI) with solid reactor-walls is inevitable. The interaction between these two extreme phases of matter cools down the plasma and damages the wall, both of which are unfavourable in terms of achieving a steady-state fusion reactor plasma with central temperatures of 150 million degrees, while maintaining the integrity of the first wall. Essentially, fusion energy research is about learning how to tame a star in a chamber which consists of available materials. Sufficient methods to produce the star are known already, but designing such a chamber is challenging.

The Joint European Torus (JET) tokamak, which started operating in 1983, is currently the largest magnetic confinement plasma physics experiment in the world. Since 1983, it has been one of the main devices worldwide in establishing the know-

ledge required for building a fusion reactor. During the 2010 – 2011 shutdown, the previous *plasma-facing components* (PFCs) of JET, consisting of *carbon-fibre composites* (CFC), were replaced with full metal ones of tungsten and beryllium [3]. This is the wall configuration foreseen in the activated operational phase of the International Thermonuclear Experimental Reactor (ITER) tokamak [4], [5]: the next major fusion experiment foreseen to go into operation in 2019. Thus, the present *ITER-like wall* (ILW) JET offers critical insight into plasma-surface interaction and plasma operation anticipated in the ITER.

In this study, erosion and transport of tungsten in JET type-I ELMy H-mode plasmas are simulated. The type-I ELMy H-mode is foreseen as one of the principal, high-performance operation regimes in the future fusion reactors. While tungsten is more resilient than CFC to erosion caused by plasma-surface interaction, as a plasma impurity, it may considerably impair the plasma performance by increasing the radiation losses. In fact, it has been deduced that a tungsten particle-concentration of one tenth of a per-mille can prevent the self-sustaining plasma-operation, thus ruling out the possibility of a practical fusion reactor [6]. Therefore, it is especially important to understand the tungsten contamination process in the fusion reactor-relevant H-mode plasmas in fusion devices operating with tungsten PFCs. Tungsten erosion and transport are simulated, in this study, with the quasi-kinetic Monte-Carlo test particle code DIVIMP [7] on background plasmas calculated and dynamically evolved in time with the 2-D multi-fluid code EDGE2D/EIRENE [8 ,9 ,10].

This report is divided into five chapters. The first chapter introduces the basics of the controlled nuclear fusion with the emphasis on the magnetic plasma-confinement. The second chapter explains the phenomena of edge plasmas and plasma-surface interaction, as well as the modelling methods used for edge plasmas. In the third chapter, the simulated JET plasma discharge is described and compared to the background plasma simulations obtained with EDGE2D/EIRENE. The fourth chapter concentrates on the tungsten erosion and transport simulation results obtained with DIVIMP, and, finally, the fifth chapter concludes this report.

1 Controlled Nuclear Fusion

1.1 Thermonuclear Fusion

In a nuclear fusion reaction, two nuclei fuse together to form a heavier one. The mass defect, Δm, associated with the change in the total nuclear binding energy, is converted to energy according to the equation $E = \Delta mc^2$ [11], where c stands for the speed of light. This way, net energy can be gained by fusing elements until iron, Fe (A=56), i.e. the element with the highest binding energy per nucleon, is obtained.

For the fusion reaction to occur, two nuclei must be brought within the range of the attractive nuclear force: $\sim 10^{-15}$ m. Positively charged nuclei experience, however, a strong electromagnetic repulsion, i.e. *Coulomb barrier*, which they must overcome first. To do so, they must approach each other with high relative velocity, which in thermonuclear fusion is achieved by heating the fuel up to the range of 10^8 Kelvins. At these temperatures, a sufficient fraction of the fuel nuclei can penetrate the Coulomb barrier to produce reactor-relevant fusion yields. At this required temperature range, a notable fraction of the electrons can overcome the attractive potential of the nuclei, thus ionizing the gaseous fuel. This ionized gas is called *plasma*. Therefore, plasma physics plays a major role in the fusion research.

The lowest required temperature for reactor-relevant fusion yields is obtained with a fuel-mixture of deuterium (D) and tritium (T). They provide the largest possible thermonuclear fusion rate of about 10^{-21} m^3/s, calculated by assuming an even fuel mixture and Maxwellian velocity distribution [12]. The D-T reaction rate peaks at the relatively low temperature of 50 keV, and already at the range of 10 – 20 keV ($\sim 150 \cdot 10^6$ K) the rate is sufficient for a fusion reactor. The temperature here is given in units $T_{\mathrm{eV}} = k_{\mathrm{B}} \cdot T_{\mathrm{K}}$, where k_{B} is the *Boltzmann* constant. This convention is used in this study from now on. Other feasible fusion fuel mixtures are D-D and D-He^3 [12]. D-D fuel mixture is likely to be used in the second generation fusion reactors due to abundance of deuterium and radioactivity issues related to tritium.

A D-T fusion reaction produces an α-particle of 3.5 MeV and a neutron of 14 MeV [12]. Although the energy gained in a D-T reaction is significant, a fusion reactor requires also a considerable energy input to obtain the required temperatures of 10 – 20 keV. To produce net energy, the thermal output from the reactor must exceed the total heating power, which has to compensate the losses caused by convection, conduction and radiation. This can be written in terms of a gain factor, Q, defined as the ratio of the thermal fusion power to the applied heating power [13].

The highest achieved gain factor so far has been 0.65 [14] with JET, and one of the primary goals of the ITER project is to achieve $Q = 10$ [15]. In suitable conditions, the 3.5 MeV fusion α-particles can provide sufficient heating power to overcome the power losses, thus *igniting* the plasma: $Q \to \infty$. The criterion for a pure, evenly distributed, and spatially constant D-T plasma to ignite can be summed up into a *triple product* (also known as the *fusion parameter*). The minimizing value of this criterion occurs at the ion temperature of $T = 15$ keV. At this temperature, the ion density, n [m^{-3}], and the energy confinement time, τ_E [s], must satisfy $nT\tau_E > 8.3$ atm s (atm $\approx 10^5$ Pa) [13]. Therefore, achieving ignition requires confinement of high enough fuel-pressure for a sufficiently long duration.

The confinement strategies in the controlled nuclear fusion can be divided into inertial and magnetic confinement. In the inertial confinement, one imposes very high pressures of $p > 10^{11}$ atm ($n > 10^{31}$ m^{-3}, $T \sim 10$ keV) for a short duration ($\tau_E < 10^{-10}$ s) by heating a D-T pellet with strong photon beams. The surface of the pellet vaporizes immediately and, while expanding, causes an inward compressing shock wave, which drives the central pressure of the pellet over the ignition criterion [16]. The confinement is provided by the inertia of the particles of the exploding pellet. In the magnetic confinement, on the other hand, one aims to achieve a steady-state ($\tau_E \sim$ several s) reactor-operation by confining a low pressure ($p \sim 1$ atm, $T \sim 15$ keV, $n \sim 10^{20}$ m^{-3}) plasma fuel with strong magnetic fields [12].

1.2 Magnetic Confinement – Tokamak

Magnetic plasma-confinement is based on the *Lorentz* force affecting a charged particle in an electromagnetic field [13]. According to the Lorentz force, charged particles are accelerated parallel to electric field, **E**, and confined into gyro motion perpendicular to magnetic field, **B**. The centre of the gyro-motion is called the *guiding-centre*. Accordingly, a magnetic field greatly reduces the transport of charged particles perpendicular to it, which leads to plasma confinement in two out of the three spatial co-ordinates. The last direction, where the plasma must be confined, is the parallel-**B** one. In tokamaks this is accomplished by winding the magnetic field up to itself, thus eliminating the straight parallel-**B** losses. The ratio of the parallel-**B** guiding-center velocity to the perpendicular-**B** one is typically of the order of 10^5 in tokamaks. Therefore, fuel particles have to travel a distance of the order of 10^5 times the plasma's minor radius (figure 1a, component *a*) before reaching the plasma-facing components.

A tokamak is a toroidal system, in which the plasma is confined by a helical

magnetic field in a vacuum chamber (figure 1). The geometry of the vacuum chamber is characterized by the major radius, R, the minor radius, a, and the elongation, i.e. the ratio of the vertical radius, b, of the vacuum chamber to its horizontal one (figure 1a). These parameters and the related plasma volumes for JET and ITER are presented in the table 1 [17]. The linear dimensions of ITER are roughly double to those of JET and the plasma volumes differ roughly by a factor of 9 [17].

Table 1: The approximative geometrical parameters of the vacuum chambers of JET and ITER. R stands for the major radius, a for the minor radius, b/a for the elongation and V for the plasma volume.

	JET	ITER
R	3 m	6.2 m
a	1.2 m	2 m
b/a	1.7	1.7
V	100 m^3	840 m^3

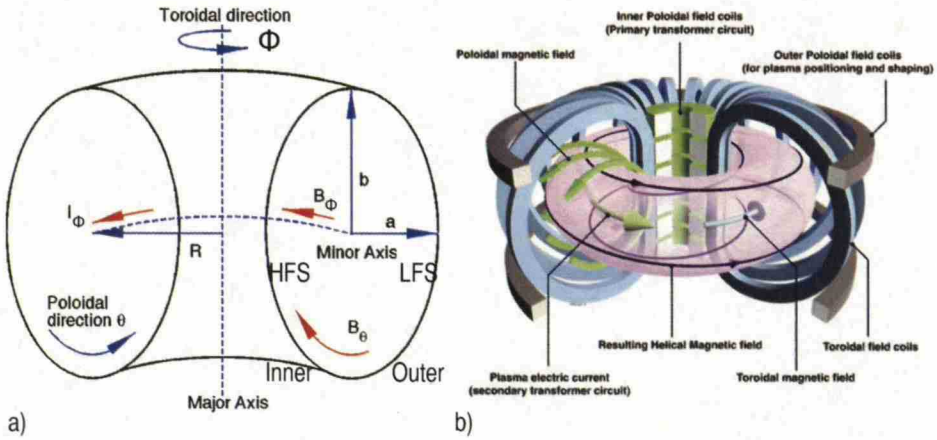

Figure 1: a) The used co-ordinate system. b) Schematic of a tokamak, courtesy of EFDA-JET [18]

The primary component of the magnetic field in a tokamak is the *toroidal* one, B_Φ, which is generated by toroidal field coils (figure 1). The toroidal field cannot, however, confine the plasma by itself. The magnitude of the toroidal field varies as $B_\Phi \propto R^{-1}$. This leads, through guiding-centre drifts, to separation of opposite charges and to formation of a vertical electric field in the plasma. The electric field leads to an outward $\mathbf{E} \times \mathbf{B}$ drift, thus ultimately deteriorating the confinement [12]. To short-circuit this electric field, a *poloidal* magnetic field, B_θ, is also required. B_θ is generated by imposing a toroidal current, I_Φ, into the plasma. In addition to the toroidal current, the poloidal field is shaped and positioned by outer poloidal field coils. Altogether, the resulting magnetic field of a tokamak is a helical one. B_θ is usually of the order of $0.1B_\Phi$, which leads to a small *magnetic pitch angle* B_θ/B_Φ.

The magnetic pitch angle in a tokamak is typically written in terms of a *safety factor*, q_s, which is defined as the number of toroidal circuits a field line completes within a full poloidal revolution. Due to the magnitude variation of the toroidal magnetic field, the inner side of the poloidal cross-section of a tokamak is often called the *high field side* (HFS) and the outer side the *low field side* (LFS) (figure 1a). The half-height of the poloidal cross-section is called the *mid-plane*.

To obtain a steady-state magnetic equilibrium in a tokamak, the magnetic force must balance the plasma pressure [12]: $\mathbf{J} \times \mathbf{B} = \nabla p$. The $\mathbf{J}$ stands for the current density in the plasma. Accordingly, $\mathbf{B}$ must be perpendicular to the pressure gradient: $\mathbf{B} \cdot \nabla p = 0$. Therefore, the helical field lines map nested toroidal surfaces of constant pressure. The centre of these surfaces, which approaches a single field line with maximum pressure, is called the *magnetic axis* [19]. The poloidal magnetic flux, $\Psi_p = \int \mathbf{B} \cdot \mathbf{dA}$, that flows through a toroidal pressure contour, $\mathbf{dA}$, is constant and depends only on p [19]. Accordingly, Ψ_p can be used as a radial flux surface co-ordinate, which is usually normalized to 0 at the magnetic axis and to 1 at the *last closed flux surface* (LCFS).

The shape of the poloidal magnetic equilibrium in a tokamak can be determined with geometrical parameters of the LCFS: horizontal width, elongation and *triangularity*, δ. δ represents the horizontal dislocation of the highest or the lowest point of the LCFS field line from the core centre [12]. δ is usually presented as a fraction of the core's half-width. A positive triangularity stands for dislocation towards the centre of the torus. Figure 2 illustrates first open flux surfaces of high and low upper-triangularity magnetic equilibriums at JET.

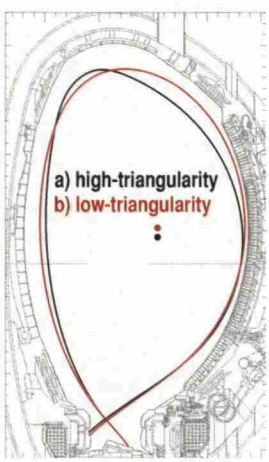

Figure 2: Poloidal magnetic equilibriums of high- and low-triangularity at JET: a) $\delta \sim 0.4$, b) $\delta \sim 0.2$. The magnetic axes are illustrated with dots.

The operational parameter space and ultimately the confinement of a tokamak

is limited by magnetohydrodynamic (MHD) instabilities, which are predominantly formed on rational q_s surfaces. The density limit disruption [12], for instance, generally restrict the operational space to electron densities below a certain limiting value. This value has been observed to correlate well with the empirical *Greenwald* limit [20].

The magnetic confinement efficiency can be written as the ratio of the plasma pressure to the *magnetic pressure*: $\beta = p^2/(B^2/2\mu_0)$. The achievable β is the economical figure of merit for a specific magnetic confinement device. The high β plasmas are, however, susceptible to MHD instabilities, and a maximum limiting value for β has been observed and documented in [21].

The radial extent of plasma in a vacuum chamber is limited by interaction with plasma-facing components (PFCs). The LCFS is the last flux surface not in contact with the PFCs, and the flux surfaces beyond the LCFS are open. The region of the open field lines, within which the wall sink action scrapes the plasma off, is called the *scrape-off layer* (SOL) (figure 3). The LCFS can be specified either by a solid limiter intersecting the outermost flux surfaces or by a diverting magnetic field, which forms a separating flux surface called the *separatrix*. The first is called the *limiter* and the latter the *divertor* configuration. Modern tokamaks operate principally on the divertor configuration, and the remaining of this study concentrates on that one. Further information about the limiter configuration can be found in [23].

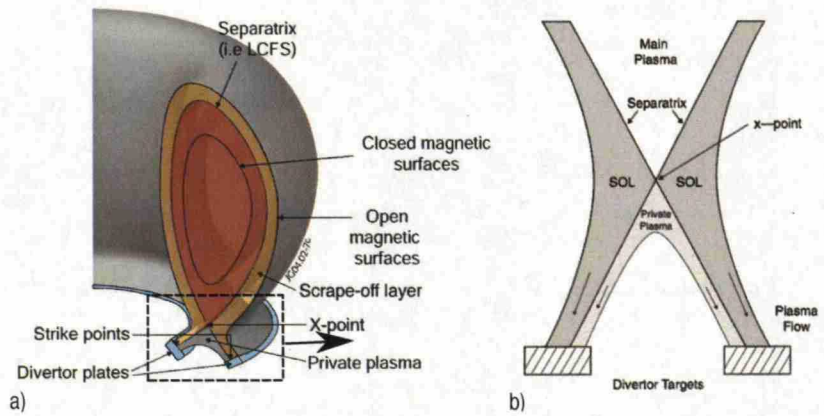

Figure 3: a) The magnetic equilibrium geometry of a divertor configuration, courtesy of EFDA-JET [22]. b) X-point geometry of a divertor [23]

The divertor components in contact with the plasma are called the *divertor targets* (figure 3a). The locations where the separatrix intersects the targets are called the *strike points*. The LFS target is often also called the *outer target* (OT) and the HFS target the *inner target* (IT). In the divertor configuration a poloidal magnetic

null, called the *X-point*, is formed (figure 3b). The plasma region restricted by the separatrix and the X-point is called the *private flux region* (PFR).

1.3 Plasma Impurities

Ideally, a fusion plasma would contain only hydrogenic species (D-T), i.e. atomic number $Z = 1$. Such conditions are, however, unrealistic. At least helium ash ($Z = 2$), originating from the D-T fusion reactions, is present. In addition, plasma-surface interactions are inevitable and lead to release of atoms and molecules from the solid surfaces by evaporation and sputtering. Impurities may also be puffed into the reactor for diagnostic purposes as well as for mitigating heat loads to the PFCs. Therefore, plasma impurities are an intrinsic part of the magnetic confinement fusion, which needs to be studied and understood to minimize their harmful consequences while optimizing the beneficial ones. [23]

Impurities cause fuel dilution, increased radiation and increased erosion of PFCs. The principal harmful consequence of the plasma impurities is cooling of the main plasma by increased radiation and fuel dilution, thus deteriorating the energy confinement and lowering the fusion power. In the fuel dilution process, impurities contribute to the total plasma pressure, which is limited below the Troyon β -limit [21]. Therefore, the impurities replace fuel particles, and this drawback cannot be overwhelmed by increasing the fuel density. [23]

The increased radiation is the principal plasma-cooling effect caused by impurities. In the coronal equilibrium (see [24], p. 225, for definition), the radiated power density caused by a given impurity species can be written:

$$P_Z^{\mathrm{rad}} = n_e n_Z R_{\mathrm{rad.}}, \tag{1}$$

where n_e stands for the electron density, n_Z for the impurity density and $R_{\mathrm{rad.}}$ for the radiation power function [12]. The radiation power function varies greatly among elements (figure 4.25.1 in [12]). Plasma impurities increase the radiation losses by enhancing the bremsstrahlung radiation, which scales as $P_{\mathrm{rad}}^{\mathrm{brehm}} \propto Z_{\mathrm{eff}}^2$, and by radiation through atomic processes, i.e. recombination and line radiation. The Z_{eff} stands for the average charge state of the plasma. The radiation through the atomic processes is the dominant cause of increased radiation. Consequently, the high atomic number elements are much more harmful for the energy confinement than the low atomic number species. Tungsten (W, $Z = 74$), for instance, is roughly 1000 times stronger radiator than carbon (C, $Z = 6$) in the fusion relevant temperatures of 10 – 20 keV (figure 4.25.1 in [12]). Low Z impurities, such as carbon, become fully

stripped of their orbital electrons at those temperatures, whereas high Z impurities, such as tungsten, retain some of their orbital electrons throughout the entire fusion relevant temperature range. Core tungsten concentrations of about $1.9 \cdot 10^{-4}$ ($c_W = n_W/n_e$) are estimated to prevent ignition, while the minimum triple product (see the section 1.1) for ignition is increased by 20% in the case of $c_W \approx 3 \cdot 10^{-5}$ [6].

The enhanced radiation due to impurities is not, nevertheless, solely unfavourable. In the SOL relevant temperatures, < 100 eV, the low Z impurities retain some of their orbital electrons, thus providing a considerable radiative capability. Therefore, non-intrinsic low Z impurities, such as neon and nitrogen, are often puffed into the plasma to mitigate the heat loads to PFCs. This is called SOL plasma *seeding*.

Erosion of PFCs is one of the fundamental challenges in the magnetic confinement fusion. While the process causes release of plasma impurities, it also limits the lifetime of the PFCs. While tungsten is more resilient against erosion due to hydrogenic species than CFC, the erosion due to plasma impurities may still be significant. This follows from the more efficient momentum transfer and higher surface impact energy of the plasma impurities due to their higher mass and charge state. The latter effect follows from an electric field between the plasma and solid surfaces. This electric field gives energy to the particles according to their charge state. The formation of this electric field is explained in the section 2.1.

1.4 Plasma-Facing Materials

The material selection as well as the design of the PFCs is one of the key research areas in the magnetic confinement fusion. The PFC materials have proven to affect the plasma properties and the performance of the experimental fusion devices [25].

The PFCs of the very first tokamaks consisted mainly of non-refractory medium Z materials, such as steel. Coupled with poor vacuum conditions and imperfect magnetic field alignment, this resulted in impurity radiation accounting for almost all the energy loss from the core plasma, thus limiting the energy confinement to low values. Later, confinement was improved by advanced vacuum technology, enhanced magnetic field control, and refractory materials, such as tungsten, in limiters and divertor targets. In 1978, in a neutral beam injection (NBI) experiment on Princeton Large Torus tokamak operating with tungsten limiters, centrally peaked radiation was observed, and the maximum ion temperatures were limited to 2 keV [25]. Replacing the tungsten with carbon, and conditioning main wall with titanium between discharges, enabled achievement of record ion temperatures of 7 keV [25]. Since those days, low Z materials, especially carbon, have been widely employed for PFCs. [23]

Carbon PFCs have demonstrated an excellent operational flexibility. Being low Z, the eroded carbon mitigates automatically the target heat loads by increasing the edge plasma radiation. Carbon PFCs show, however, significant tritium retention when operating in D-T. Tritium is β^- active with the half-life of 12.3 years. In reactor scale devices, the tritium inventory inside the machine may accumulate significant enough to become a safety concern for the population outside the reactor area. With carbon PFCs, the re-deposition trapping of tritium in form of carbon-hydrates can cause tritium accumulation well beyond the safety-limits. For ITER, a safety limit of 1 kg of retained tritium inside the reactor has been decided, thus imposing an operational upper limit of 700 g [26]. Using carbon PFCs, ITER is predicted to reach this ceiling within a few hundred full performance shots [26]. Therefore, despite the beneficial properties of the carbon, the high Z refractory materials, such as tungsten, have reclaimed their position as the principal PFC materials in tokamaks.

Tungsten has the highest surface binding energy (8.8 eV) of all elements, which gives tungsten beneficial resiliency to sputtering. It is, however, considerably brittle, which greatly limits the bearable heat flux densities for tungsten PFCs. In fact, a steady-state wall heat flux density on tungsten PFCs cannot exceed 10 MW/m^2 in order to avoid excessive damage and melting of the components [17]. Meeting this requirement in ITER during the activated operational phase is one of the major challenges faced by the project. Furthermore, due to the detrimental effect of tungsten impurity for the core performance, a careful divertor impurity screening control is required for tokamaks operating with tungsten.

In the current baseline, the ITER PFC materials consist of beryllium main chamber limiters, tungsten divertor baffles and carbon-fibre composite (CFC) divertor strike points [15] (figure 4a). Prior to the D-T campaigns, the divertor PFCs in ITER are foreseen to be switched to full tungsten ones to prevent excessive accumulation of retained tritium [28]. The beryllium functions as a low Z non-carbon main chamber material. During the 2010 – 2011 shutdown, the previous CFC PFCs of JET were replaced with ITER-like ones consisting of bulk beryllium main chamber limiters, bulk tungsten outer strike point and tungsten coated CFC elsewhere in the divertor [3, 29] (figures 4b and 5).

The scientific evolution of the PFC materials has raised tungsten and beryllium as the principal first-wall materials for the future fusion reactors. The major question, which will be partially answered during the JET ITER-like wall campaigns, is whether these materials will provide sufficient operational flexibility for the high performance, $Q > 10$, operation in ITER. The achievement of high Q re-

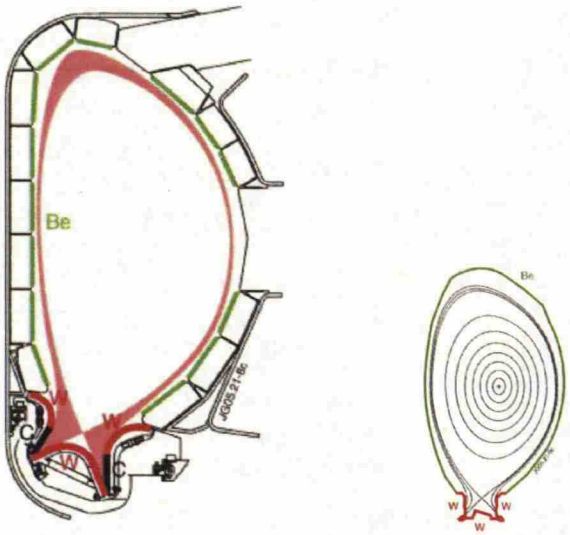

(a) (b)

Figure 4: a) The ITER wall configuration chosen for the non-nuclear campaigns. b) The JET ITER-like wall configuration. Figures are modified from [27].

(a) (b)

Figure 5: a) The JET tokamak after the installation of the ITER-like wall on the 8th May 2011. Modified from [3]. b) The ITER-like wall diveror configuration of the JET tokamak with the magnetic field geometry modelled in this study. The outer strike point is situated on the tile number 5, which is the bulk tungsten one. The purple tiles in the figure represent the 200 μm vacuum plasma spray (VPS) tungsten coated CFC tiles, and the pink ones stand for the 10 μm combined magnetron sputtering and ion implantation (CMSII) tungsten coated CFC tiles [29].

quires plasma operation within a high confinement mode (H-mode) with frequent transient events called edge localized modes (ELMs), which impose excessive temporal heat loads on the target plates. This increases the risk of damage of the PFCs.

1.5 High Confinement Mode

To achieve the required temperatures, a fusion reactor demands a substantial power input. Unfortunately, the energy confinement time, τ_E, has been found to decrease with the applied heating power, thus limiting the heating efficiency. Fortunately, a sudden transition to enhanced confinement has been observed to occur when the power crossing the separatrix exceeds a certain threshold value [30]. In this *high confinement mode* (H-mode), the τ_E is typically twice as long as in the previous *low confinement mode* (L-mode). In JET, the L-H power threshold is usually around 5 – 8 MW, whereas for ITER, a value around 52 – 86 MW has been estimated [31].

The appearance of the H-mode is associated with a sudden increase in the edge pressure gradient. Accordingly, an *edge transport barrier* (ETB) and a pressure *pedestal* are formed, and the edge deuterium recycling rate interpreted from the D_α signal is decreased [32]. D_α measures the intensity of the α Balmer line emitted by neutral hydrogenic particles entering the plasma [12]. The formation of the ETB is associated with a suppression of the edge plasma turbulence, which, presumably, predominantly drives radial convective transport within the edge plasma. The suppression of the turbulence is related to $\mathbf{E} \times \mathbf{B}$ velocity shear with a favourable magnetic shear, thus suppressing the formation of large turbulent eddy structures [33]. These structures could, otherwise, serve as channels for direct convective transport.

After the formation of the ETB, the density and the temperature of the entire core plasma are increased, as the pedestal values determine the boundary conditions for the core plasma. In fact, ITER is foreseen to require pedestal top temperatures of about 4 keV to obtain the central plasma conditions necessary for the $Q_{\text{D-T}} = 10$ operation [17]. Therefore, H-mode is mandatory for achieving the pedestal gradients required for the high performance operation.

The steep H-mode pedestal gradients are susceptible for MHD instabilities. These MHD instabilities, called *edge localized modes* (ELMS), lead to sudden collapses of the pedestal driving significant particle and heat fluxes to the SOL plasma. They can be identified as D_α peaks caused by enhanced wall recycling. The ELMs do not, however, deteriorate the central plasma confinement significantly. Instead, the ELM influence usually terminates at the depth of 20% of the minor radius [34]. The pedestal rebuilds rapidly after the restoration of the ETB, thus providing conditions for a following ELM, therefore leading to periodic ELMs. The ELM frequencies, f_{ELM}, are usually within the range of about 1 Hz – 1000 Hz [34].

The most common ELM types are *type-I* and *type-III*. These can be categorized by their power dependencies [35]. In the type-III ELM regime the ELM frequency has been observed to decrease and in the type-I ELM regime to increase with in-

creasing input power [35]. The type-III ELM regime is observed to occur when the input power is slightly above the L-H threshold [34]. The type-III ELMs are associated with resistive MHD instabilities [36]. They are characterized by high frequencies and small amplitudes: 0.1 – 1 kHz, $\Delta W_{\mathrm{ELM}}/W_{\mathrm{ped}} \sim 1\%$ [23]. Increasing the input power well above (>20%) the L-H threshold leads to a short ELM-free period followed by the type-I ELM regime [34]. The type-I ELMs are considered to be driven by ideal MHD peeling-ballooning mode instabilities [36], triggered when a critical edge pressure gradient is exceeded. The type-I ELMs are characterized by small frequencies and large amplitudes: 1 – 100 Hz, $\Delta W_{\mathrm{ELM}}/W_{\mathrm{ped}} \sim 3 - 20\%$. In addition to these, a variety of ELMs, such as type-II, grassy, and type-V, have been observed [34]. These are, however, beyond the scope of this study and are not described here. A more detailed description of ELMs can be found in [34].

Although the type-I ELMs have large amplitudes, the type-I ELM regime offers excellent performance in terms of the triple product (see the section 1.1) [34]. While the ELM-free H-mode regimes provide high energy confinement, they generally suffer from unacceptable impurity accumulation in the core plasma. Therefore, ELMs are necessary to avoid excessive impurity contamination by purging the core of impurities. Thus, the type-I ELMy H-mode is currently foreseen as one of the principal high-performance operation regimes in the fusion reactors.

The rapid release of the pedestal stored energy into the SOL may constitute a serious threat to the PFCs. In ITER, the maximum allowable energy loss of 1 MJ per ELM has been calculated [37]. In the $Q_{\mathrm{D\text{-}T}} = 10$ operation, this is associated with a fractional loss of only less than 1% of the *pedestal stored energy* [38]:

$$W_{\mathrm{ped}} = \frac{3}{2}\left(n_{\mathrm{i,\,ped}} T_{\mathrm{i,\,ped}} + n_{\mathrm{e,\,ped}} T_{\mathrm{e,\,ped}}\right) V_{\mathrm{plasma}}, \tag{2}$$

whereas the observed ELM magnitudes in the type-I ELMy H-mode plasmas span from 3% to 20% [34]. V_{plasma} stands for the volume of the confined plasma.

The ELM energy and particle fluxes from the pedestal to the SOL plasma arise predominantly at the LFS outer mid-plane (OMP) region consistent with the peeling-ballooning MHD characteristics for the ELMs [34, 39, 40, 41]. A typical ELM duration, τ_{ELM}, defined as the duration of the magnetic fluctuation phase, have been observed to be around 100 – 200 μs [34]. ELMs have been observed to eject radially and poloidally finite *filamentary* structures with a radial velocity of the order of 600 m/s and a poloidal spreading of about 500 m^2/s [42]. The filamentary structures are observed at the OMP roughly within the first 100 μs after the ELM onset, which is defined as the foot of the rapid increase of the D_α signal in the

divertors [43]. After crossing the separatrix, the filament loses its energy through the parallel-**B** transport to the solid surface. The fraction of the total ELM energy, ΔW_{ELM}, reaching the main chamber wall has been found to be in the range 3 – 30% and scale proportionally to the distance of the outer limiter from the separatrix [38, 44].

The ELM losses can be divided into groups defined by the dominant transport processes: *convective*, $\frac{3}{2}\Sigma_j \Delta n_j T_j$, and *conductive*, $\frac{3}{2}\Sigma_j n_j \Delta T_j$. The total ELM magnitude can be written [43]:

$$W_{\mathrm{ELM}} = \frac{3}{2}\int_{V_{\mathrm{plasma}}} \left[\Sigma_j \Delta n_j T_j + \Sigma_j n_j \Delta T_j - \Sigma_j \Delta n_j \Delta T_j\right] dV, \tag{3}$$

where the cross-term is subtracted. The convective losses appear to depend only weakly on the plasma parameters, being roughly $\Delta W_{\mathrm{conv}}/W_{\mathrm{ped}} \sim 4 - 8\%$ for a large region of the operational space [43]. The conductive losses, on the other hand, have been observed to increase from $\Delta W_{\mathrm{cond}}/W_{\mathrm{ped}} \sim 5\%$ to $\Delta W_{\mathrm{cond}}/W_{\mathrm{ped}} \sim 20\%$, as the *neoclassical electron collisionality at the pedestal* decreases from $\nu_{\mathrm{e}}^{*} \sim 0.5$ to $\nu_{\mathrm{e}}^{*} \sim 0.1$ [43]. This parameter can be written [43]:

$$\nu_{\mathrm{e,\,ped}}^{*} = R q_{95} \varepsilon^{-3/2} (\lambda_{\mathrm{e,\,e}})^{-1} \propto \frac{n_{\mathrm{e,\,ped}}}{T_{\mathrm{e,\,ped}}^{2}}, \tag{4}$$

where q_{95} stands for the safety-factor at the 95% flux surface, $\varepsilon = a/R$, and $\lambda_{\mathrm{e,\,e}}$ represents the electron-electron Coulomb collision mean free path [45]. Consequently, the ratio of the convective ELM losses to the conductive ones is foreseen to increase as a function of the plasma collisionality, and the total ELM magnitude to decrease accordingly.

It should be noted that the energy terms in the equations (2) and (3) are given in units eV for simplicity. In the following sections, these will be generally converted to Joules.

2 Scrape-off Layer

The scrape-off layer connects the hot ($> 10^7$ K) confined plasma with the solid first wall ($\sim 10^2$ – 10^3 K). The main practical objective in researching the SOL is to establish techniques to attenuate wall power loads and to screen wall-released impurities from leaking to core while ensuring as high as possible core boundary temperature and density. While the length scale of the core plasma is within metres, the typical width of the SOL is measured in centimetres only. Therefore, the power from the metre-scale core is largely channelled to the solid surface via a centimetre-scale plasma-slice, which may impose surface heat fluxes greatly beyond existing engineering limits. Thus, reaching these objects requires a careful design of the control parameters, such as machine geometry, wall configuration, plasma operation and impurity seeding.

2.1 Plasma Sheath

The plasma is electrically *quasi-neutral* ($n_e \approx \Sigma_i n_i Z_i$). Electrical conductivity in fusion plasmas is typically very high: about 10^7 – $10^9/\Omega$m [12, 46]. Therefore, any significant charge separation results into extremely high currents rapidly equilibrating the potential difference. A characteristic scale-length for spontaneous charge separations in plasma is given by the *Debye length* [12]:

$$\lambda_{\text{Debye}} = \sqrt{\frac{\varepsilon_0 T_e}{n_e e^2}}, \tag{5}$$

where ε_0 represents the vacuum-permittivity, T_e the electron temperature, n_e the electron density, and e the unit charge. Typically in tokamaks λ_{Debye} is of the order of 10^{-4} m.

The quasi-neutrality is not, however, satisfied everywhere in the plasma vessel. Instead, a thin region ($\sim 5\lambda_{\text{Debye}}$) of net charge, called the *sheath*, forms spontaneously between the plasma and the solid surface. The lower mass electrons reach the surface easier than the heavier ions, thus charging the wall negatively. As a consequence, a steady-state ambipolar electric field arises to accommodate the inertia difference to maintain a zero net outflow of charge from the plasma.

The sheath has a significant influence to the physics in the SOL by imposing the PSI boundary conditions. According to the generalized Bohm criterion [47, 48], an ambipolar plasma flow at the sheath edge (SE) reaches the sonic velocity: $v_{\text{SE}} \geq c_s = \sqrt{(T_e + T_i)/m_i}$. For an isothermal flow, $v_{\text{SE}} \leq c_s$ is required in the plasma [23]. This leads to the boundary condition for the plasma flow at the sheath

entrance: $v_{SE} = c_s$.

All the ions reaching the sheath edge will reach the wall which is absorbing [23]. Therefore, the ion flux reaching sheath edge, Γ^i_{SE}, and the wall, Γ^i_w, can be written:

$$\Gamma^i_w = \Gamma^i_{SE} = n_{SE} c_s, \tag{6}$$

where n_{SE} represents the plasma density at the sheath edge. The equation (6) gives the quantification of the plasma sink action caused by the PSI.

The potential difference between the wall and the plasma, V_{sf}, can be estimated by relating the ion and the electron flux densities at the wall. In floating conditions, i.e. the surface is not electrically biased, the fluxes at the wall must be equal. For hydrogenic plasmas, using the equation (6) for ions and assuming for electrons a one-way random Maxwellian flux attenuated by the Boltzmann relation leads to [23]:

$$\frac{eV_{sf}}{T_e} = 0.5 \ln \left[\left(2\pi \frac{m_e}{m_i} \right) \left(1 + \frac{T_i}{T_e} \right) \right]. \tag{7}$$

For hydrogenic plasmas, the equation (7) gives $eV_{sf}/T_e \approx -3$ [23].

In addition to a particle sink, the sheath is also a power sink. The *sheath heat transmission coefficients* for electrons, γ_e, and ions, γ_i, represent the amount of energy that is removed from the population per particle entering the sheath. Therefore, the total parallel-**B** heat flux density entering the sheath can be written:

$$q_{tot} = q_e + q_i = \gamma_e T_e \Gamma_{SE} + \gamma_i T_i \Gamma_{SE}. \tag{8}$$

Assuming power conservation within the sheath, this must be equal to the parallel-**B** heat flux density reaching the surface: $q_{surface} = q_{tot}$. The individual contributions of ions and electrons do not, however, remain the same through the sheath. Instead, the electrons transfer energy to the ion population through the sheath potential. [23]

Calculating the sheath heat transmission coefficients requires a detailed knowledge about the parallel-**B** velocity distribution and about the electric fields within the SOL. Calculating these in reactor scale simulations would be an overwhelming task for modern computers; accordingly, the models typically employ ready-made kinetic calculations. A variety of γ_i and γ_e values have been obtained: $\gamma_i \sim 1.5 - 3$ [23] and $\gamma_e \sim 4.5 - 5.5$ [49] . The numbers used in this study are the ones suggested in [23]: $\gamma_i = 2.5$ and $\gamma_e = 4.5$.

So far, a surface normal parallel to **B** has been assumed. In fusion reactor applications, the angle between the surface normal and **B** is usually, however, very oblique: $\sim 89°$. To first order the obtained boundary conditions are, nevertheless,

not affected [50]. Therefore, the values obtained here are assumed to provide sufficient approximations for the research conducted in this study.

2.2 Plasma Fluid Modelling

Plasma transport is a kinetic phenomenon, i.e. it happens in a six dimensional phase-space. Let $f_\sigma(\mathbf{x},\mathbf{v},t)$ be the phase-space density of a particle species σ. The time-evolution of this phase-space density is given by the kinetic equation [49] :

$$\mathbf{D}_\sigma f_\sigma = \left(\frac{\partial}{\partial t} + \mathbf{v}\cdot\nabla_x + \frac{Z_\sigma e}{m_\sigma}(\mathbf{E}+\mathbf{v}\times\mathbf{B})\cdot\nabla_v\right) f_\sigma = \sum_{\varsigma\in\{\mathrm{i,e,n},Z\}} \mathbf{C}_{\sigma\varsigma} + \mathbf{S}_\sigma, \quad (9)$$

where $\mathbf{D}_\sigma$ represents a phase-space derivative for species $\sigma \in \{\mathrm{e,i,n},Z\}$, Z represents impurity species, n neutrals, $\mathbf{C}_{\sigma\varsigma}$ the $\sigma-\varsigma$ collision operator, and $\mathbf{S}_\sigma$ a volumetric source. Solving the equation (9) would provide the time-evolution of the phase-space density and the solution for the plasma. Solving the equation (9) in fusion reactor scale applications is, however, well beyond the computational capability of the modern computers. Therefore, a set of simplified equations, following only the velocity moments of the equation (9), are typically used. The velocity moments yield a non-closing series of fluid equations. The hierarchy of the fluid equation is usually truncated at the level of the third (energy flux) moment by employing a short mean free path expansion [51]. The velocity moments give conservation equations for the fluid quantities: density (zeroth), flow velocity (first) and energy (second).

Applying this procedure to the equation (9) together with the *Fokker-Planck* collision coefficients [12], and employing a parallel-**B** versus perpendicular-**B** (*cross-field*) co-ordinate system, yields the *Braginskii* fluid equations [52]. These form the basis of the 2-D multi-fluid SOL modelling codes, such as SOLPS [53] and EDGE2D/EIRENE [8, 9, 10]. The cross-field transport of particles and energy in the magnetically confined plasmas is poorly understood originating from plasma micro-turbulence. Therefore, cross-field transport is introduced into the fluid equations by anomalous cross-field coefficients: diffusion, $D_\perp$ [m^2/s], convection, v_{pinch} [m/s] and conduction, χ [m^2/s].

The neutral population in the plasma is, in this study, modelled with the Monte-Carlo test particle neutral code EIRENE tracking the kinetic Boltzmann transport equation for the different neutral species within the plasma [9].

2.3 Power Exhaust

The power deposited in the core plasma will reach the reactor wall through convection, conduction and radiation. The balance between these processes largely determines the wall heat flux profile and the core performance. The power crossing the separatix by convection and conduction, P_{SOL}, can be written [34]:

$$P_{\mathrm{SOL}} = P_{\mathrm{in}} - P_{\mathrm{rad}}^{\mathrm{main}} - \frac{dW_{\mathrm{plasma}}}{dt}, \tag{10}$$

where W_{plasma} stands for the plasma stored energy, $P_{\mathrm{rad}}^{\mathrm{main}}$ for the core plasma radiative power and P_{in} for the input power. In ELMy H-mode plasmas, the inter-ELM P_{SOL} is determined by the power input subtracted by the core radiative power and the power spent into increasing the plasma stored energy, whereas the intra-ELM P_{SOL} is dominated by the large negative values obtained by the $\frac{dW_{\mathrm{plasma}}}{dt}$ term.

The balance between convection, conduction and radiation as well as between the cross-field and the parallel-**B** transport in the SOL determines the heat flux to the main chamber wall and to the divertor plates. In fluid codes, the cross-field power transport is imposed by adjusting the cross-field diffusion coefficients to match measured profiles at the outer mid-plane (OMP). The parallel-**B** power transport can be written [23, 54]:

$$\begin{aligned} q_{\mathrm{e}}^{\parallel} &= q_{\mathrm{e,\,conv}}^{\parallel} + q_{\mathrm{e,\,cond}}^{\parallel} \approx \left(\frac{5}{2} p_{\mathrm{e}}\right) v_{\parallel} - K_{\mathrm{e},\parallel} \nabla_{\parallel} T_{\mathrm{e}}, \\ q_{\mathrm{i}}^{\parallel} &= q_{\mathrm{i,\,conv}}^{\parallel} + q_{\mathrm{i,\,cond}}^{\parallel} \approx \left(\frac{5}{2} p_{\mathrm{i}} + \frac{1}{2} m_{\mathrm{i}} n v_{\parallel}^2 + \pi_i\right) v_{\parallel} - K_{\mathrm{i},\parallel} \nabla_{\parallel} T_{\mathrm{i}}, \end{aligned} \tag{11}$$

where π_i stands for the parallel ion viscosity stress and the $K_{\sigma,\parallel}$ for the parallel heat conductivities. The π_i arises from the non-linear terms of the plasma pressure tensor [54]. The parallel-**B** heat conductivities can be written, employing the short collisional mean free path expansion, [23, 54]:

$$\begin{aligned} K_{\mathrm{e},\parallel} &= 3.2 \frac{n \tau_{\mathrm{e}} T_{\mathrm{e}}}{m_{\mathrm{e}}} \approx \kappa_{0\mathrm{e}} T_{\mathrm{e}}^{5/2} \approx 2000 T_{\mathrm{e}}^{5/2}, \\ K_{\mathrm{i},\parallel} &= 3.9 \frac{n \tau_{\mathrm{i}} T_{\mathrm{i}}}{m_{\mathrm{i}}} \approx \kappa_{0\mathrm{i}} T_{\mathrm{i}}^{5/2} \approx 60 T_{\mathrm{i}}^{5/2}, \end{aligned} \tag{12}$$

where the τ_{e} and τ_{i} represent the electron and ion collision times: $\tau_\sigma = \lambda_\sigma^{\mathrm{mfp}} / v_\sigma^{\mathrm{thermal}}$. The $\lambda_\sigma^{\mathrm{mfp}}$ stands for the collisional mean free path and $v_\sigma^{\mathrm{thermal}}$ for the thermal velocity of the particle species σ. According to equations (12), the plasma heat conductivity increases significantly as a function of plasma temperature, and the

electron heat conductivity exceeds the ion heat conductivity by a factor of $\sqrt{m_i}/\sqrt{m_e} \sim 2000/60$.

The heat conductivities in equations (12) are obtained by employing the short collisional mean free path expansion. The conditions for the short collisional mean free path may, however, be violated in the SOL plasmas. The rate of departure from the short mean free path conditions can be written in terms of a local *Knudsen number*, which is defined as the ratio of the collisional mean free path to the local length-scales [49]. For the short mean free path heat conductivities to be valid, the local Knudsen number needs to be well below unity. In [49] it has been deduced that as majority of the parallel-**B** heat conduction is carried by supra-thermal electrons, the short mean free path approach is expected to become invalid as soon as the maximum local Knudsen number exceeds 10^{-2}.

If the parallel-**B** collisionality is the dominant factor driving the parallel-**B** temperature gradients, i.e. $L_{\nabla T_\sigma} \propto \lambda_{\sigma\sigma}$, the heat fluxes become self-limiting, and the local Knudsen number remains limited. Therefore, in such conditions, the short mean free path heat conductivities remain valid while the collisional mean free path increases [49]. The SOL plasmas are, however, bounded systems with spatially varying sources and fields and, therefore, far from thermodynamic equilibrium. In such conditions, the linear increase of the gradient length with the mean free path cannot be guaranteed *a priori* [49]. Accordingly, in SOL plasmas, the collisional mean free path may increase while the parallel temperature gradient length remains limited, thus increasing the local Knudsen number. Employing the short mean free path heat conductivities in such conditions leads to overestimation of the conducted heat flux. In the SOL fluid codes, which, nevertheless, largely employ the short mean free path Spitzer-Härm heat conductivities [55], this discrepancy is addressed by introducing kinetic corrections in terms of heat flux limiters. In this approach, the maximum conducted heat flux is limited to the free-streaming Maxwellian flux multiplied with a factor α_σ [49]:

$$q_\sigma^{\mathrm{FL}} = \alpha_\sigma p_\sigma v_\sigma^{\mathrm{thermal}}, \tag{13}$$

where p_σ stands for the pressure. In this study, the electron and the ion heat flux limiters are set to the values suggested in [49]: $\alpha_e = \alpha_i = 1.5$.

The characteristics of the parallel-**B** power transport in the SOL determine the SOL plasma regime. These characteristics are to great extent determined by the balance between the power crossing the separatrix and the SOL density, which largely determine the SOL upstream temperature and collisionality.

The SOL plasma regime can be characterized by the SOL parallel-**B** temperature

Table 2: SOL plasma regimes

Sheath-limited	$\nabla_{\parallel} T \approx 0$	$\nabla_{\parallel} p \approx 0$
Conduction limited	$\nabla_{\parallel} T \neq 0$	$\nabla_{\parallel} p \approx 0$
Detached	$\nabla_{\parallel} T \neq 0$	$\nabla_{\parallel} p \neq 0$

and pressure profiles (table 2). The *sheath-limited* regime is characterized by low collisionality causing flat parallel-**B** temperature and pressure profiles. In this regime, the power exhaust through the SOL is mainly limited by the power absorption abilities of the plasma sheath. Increasing the SOL collisionality lowers the plasma conductivity; accordingly, a parallel-**B** gradient forms to provide a sufficient conductive power exhaust along the SOL. This regime is called the *conduction limited*. A simplified set of equations, called the *2-point model*, can be developed to describe the parallel-**B** plasma profiles in the conduction limited regime. Assuming a constant parallel-**B** pressure, a sonic flow at the sheath edge and the electron conduction carrying all the parallel-**B** power flux, $q_{\parallel}$, leads to equations [23]:

$$\begin{aligned} n_{\mathrm{u}} T_{\mathrm{u}} &= 2 n_{\mathrm{t}} T_{\mathrm{t}}, \\ T_{\mathrm{u}}^{7/2} &\approx T_{\mathrm{t}}^{7/2} + \frac{7}{2} \times \frac{q_{\parallel} s_{\parallel}}{\kappa_{0\mathrm{e}}}, \end{aligned} \tag{14}$$

where the variables labelled t represent the target values and the variables labelled u the upstream (OMP) values and $s_{\parallel}$ stands for the upstream to downstream distance.

In the *detached* regime, the balance between the upstream plasma temperature and collisionality together with the volumetric power-losses in the SOL impose target plasma temperatures lower than 2 eV. At these temperatures, the plasma-neutral collisions become significant enough to produce parallel-**B** pressure gradient in the SOL. In this regime, significant hydrogen recombination begins to occur in front of the target and the plasma ionization front detaches from the targets.

2.4 Impurity Contamination

The impurity contamination caused by PSI is determined by the combination of the impurity source magnitude, the SOL transport and the core transport (figure 6). The first provides the contamination rate, Γ^{source} [#/s], the second the core leakage fraction, f^{leakage} [%], and the third the core contamination efficiency, $\tau^{\mathrm{core}}_{\mathrm{confinement}}$ [s]. These quantities give the average amount of impurity particles confined in the core:

$$N^{\mathrm{core}}_{\mathrm{impurity}} = \Gamma^{\mathrm{source}} \frac{f^{\mathrm{leakage}}}{100} \tau^{\mathrm{core}}_{\mathrm{confinement}}. \tag{15}$$

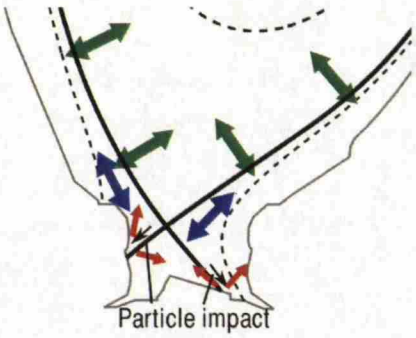

Figure 6: Schematic of the impurity contamination caused by the divertor target sputtering. The red arrows represent the target sputtering, the blue arrows the SOL transport and the green arrows the core transport.

In ELMy H-mode plasmas, all these processes vary significantly during an ELM cycle. The physical sputtering of target plates is dominated by the intra-ELM periods due to the significant heat loads. The SOL transport is heavily affected by the major variations in the SOL control parameters: temperature and density. The core confinement is predominantly limited by the ELM induced core purging.

In tokamaks operating with tungsten PFCs, the impurity source is given by physical sputtering of the tungsten plates. In the physical sputtering process, the impacting particles provide a sufficient momentum transfer to eject atoms from the surface. The sputtering magnitude depends on the projectile and the substrate materials as well as on the energy and the angle of incidence [23]. In reactor simulations, normal incidence is usually assumed. This is justified by the surface roughness [23]. The magnitude of the sputtering is described by a statistical parameter called the *sputtering yield*. The sputtering yield is defined as the average number of atoms ejected per incident particle. Tungsten has the highest binding energy of all elements and, accordingly, the highest sputtering threshold. The sputtering threshold of tungsten by deuterium impact is around 250 eV [56], whereas the sputtering threshold due to carbon impact is around 80 eV [57].

Calculating target sputtering in the simulations requires knowledge about the energy of the incident particle. As calculating the detailed ion energy distribution from first principles in reactor scale applications is well beyond the computational capability of modern computers, simplified assumptions for the impact energy are typically used. In this study, for instance, the impact energy, $E_{\text{imp.}}$, of the particles striking the solid surface is calculated using the equation:

$$E_{\text{imp.}} = 2T_{\text{i}} + 3ZT_{\text{e}}, \tag{16}$$

where Z represents the charge-state of the impacting particle. The first contribution represents the average Maxwellian one-way energy, and the latter the acceleration through the sheath potential, which is given by the equation (7): $eV_{sf} \approx -3T_e$. The initial energy of the sputtered atoms scales as $E_{eject.} \propto E_{imp.}$ [23]. Accordingly, using the equations (16), it is observed that the initial velocity of the sputtered atoms scales proportional to the square root of the plasma temperature: $v_{in} \propto \sqrt{T}$.

Once sputtered, an impurity atom will be transported as a neutral to its ionization location, beyond which its motion becomes restricted by the magnetic field. If the impurity atom ionizes within the distance of its Larmor radius from a solid surface, it will be promptly re-deposited. The prompt re-deposition fraction of tungsten can be significant ($\sim 90\%$), due to the mass-scaling of the length of the Larmor radius.

The impurity ion transport can be divided into cross-field and parallel-**B** motion. Cross-field transport of impurities is poorly understood and it is often simulated as anomalous diffusion with a coefficient spanning about $D_\perp \sim 1 - 10$ m^2/s: here, $D_\perp = 1$ m^2/s is used. The parallel-**B** force on the impurity particles is caused by collisions and by the background parallel-**B** electric field. The collisions lead to a variety of force terms, the most significant of which can be identified as the background friction, the impurity pressure gradient and forces caused by the background temperature gradients. In the fluid approximation, the parallel-**B** force on an impurity particle can be written [23]:

$$\begin{aligned} \frac{dv_Z}{dt} &= (\mathrm{FP} + \mathrm{FF} + \mathrm{FE} + \mathrm{FiG} + \mathrm{FeG}) m_Z^{-1} \\ &= -(n_Z m_Z)^{-1} \nabla_\parallel p_Z + (v_i - v_Z)\tau_s^{-1} + ZeE m_Z^{-1} + \\ &\qquad \alpha_{ec} m_Z^{-1} \nabla_\parallel T_e + \beta_{ic} m_Z^{-1} \nabla_\parallel T_i, \end{aligned} \tag{17}$$

where the first term at RHS represents the impurity pressure gradient force, the second the background ion friction, the third the electric force and the fourth and the fifth the temperature gradient forces due to electrons and ions. The α_{ec} and β_{ic} are temperature gradient force coefficients and the τ_s is the Spitzer collision time [23]. The m_Z stands for the mass of the impurity particle, E for the magnitude of the background electric field and e for the unit-charge. This equation forms the central part of the Monte-Carlo test particle code DIVIMP [7]. It has been shown in [58] that the equation (17) becomes inaccurate in the case of significant velocity difference between the impurity particles and the background plasma. In order to address this issue, an additional simulation is conducted in this study with the drift-kinetic parallel-**B** forces as suggested in [58].

The most significant of these force terms are the impurity pressure gradient

force, the ion temperature gradient force and the friction force. In the case of a target impurity source, the two first are usually directed outwards from the source location, thus enhancing the impurity leakage, and the last one towards the source location, being the principal term suppressing the impurity leakage. The friction force scales as $\mathrm{FF} \propto \tau_s^{-1} \propto n_i/T_i^{3/2}$. Therefore, the background deuterium friction decreases with decreasing plasma collisionality: $\nu_i^* \propto n_i/T_i^2$. Consequently, as the target plasma temperature increases, the initial velocity of the sputtered atoms increases, while the strength of the background friction decreases. Accordingly, the impurity leakage tends to increase with increasing target plasma temperatures as has been documented in [59].

The core confinement of impurities is determined by the cross-field transport and by the ELM induced core purging. Simulating these effects would require a core plasma transport code such as the JETTO/SANCO package [60, 61]. These simulations are, however, beyond the scope of this study. Therefore, approximative order of magnitude estimates for the tungsten core confinement time will be used instead. In JET, an upper-limit for the core confinement time is given by the Bohm diffusion [23] leading to approximately 1s. A value taking into account the effect of ELMs can be obtained by using a regression analysis based core confinement time for tungsten in ELMy H-mode plasmas documented in [62]:

$$\tau_W^{\mathrm{core}} \approx 4.0 \cdot 10^2 f_{\mathrm{ELM}}^{-1.1} \langle \tau_{\mathrm{SOL}\rightarrow\mathrm{div}} \rangle^{1.1} D_{\mathrm{SOL}}^{0.1} \qquad [\mathrm{s}], \tag{18}$$

where f_{ELM} represents the ELM frequency, $\langle \tau_{\mathrm{SOL}\rightarrow\mathrm{div}} \rangle$ the average upstream (OMP) SOL to divertor transit time, and D_{SOL} the SOL cross-field diffusion coefficient. The equation (18) has been obtained in ASDEX Upgrade [63] with full tungsten main chamber wall, whereas in JET only the divertor PFCs contain tungsten. Furthermore, the effects of the core plasma density and temperature are not included in equation (18). Accordingly, major uncertainties are imposed to the values calculated by using this equation for JET. Rough order of magnitude estimates taking into account the effect of ELMs can, however, be obtained. The SOL to divertor transit time can be estimated as $\tau_{\mathrm{SOL}\rightarrow\mathrm{div}} \sim L_{\parallel}/c_{s,\,W}$, where $c_{s,\,W}$ stands for the acoustic speed of tungsten. This is justified, as most of the tungsten flux out of the core occurs presumably during the intra-ELM phase, and the intra-ELM caused parallel-**B** pressure gradient is foreseen to lead to SOL flows comparable to the plasma sound-speed. Assuming tungsten ensemble temperature equal to the pedestal temperature, SOL diffusion coefficient of 1 m^2/s and ELM frequency of about 20 – 30 Hz gives an order of magnitude of a few 10 ms for the core confinement time. Therefore, the core confinement time is foreseen to be within the range of 10 – 1000 ms.

3 Plasma Simulations

3.1 Discharge Description

The simulations in this study are based on one of the JET ITER-like wall reference plasmas with CFC wall (figures 7 and 8): JET pulse number (JPN) 76666, $B_\Phi \approx 2.7$ T, $I_\Phi \approx 2.5$ MA, $P_{\text{input}} \approx 15.7$ MW, $n_e \sim 0.8 n_{GW}$, $\delta \sim 0.4$, $q_{95} \sim 3.5$, $f_{ELM} \sim 20$ Hz. The reader may recall the explanations for the symbols by checking the list of symbols at the end of this report. This discharge is a part of a deuterium fuelling and nitrogen seeding scan experiment at JET [64, 65]. In this series of discharges, JPN 76666 represents the lowest density reference plasma without nitrogen seeding. The plasma was fuelled with a deuterium gas puff, which was located around the inner strike point (figure 8). Edge interferometry and electron cyclotron emission measurements give the pedestal values of $n_e^{ped} \sim 6e19$ m^{-3} and $T_e^{ped} \sim 800$ eV, which determine the pedestal collisionality and the pedestal stored

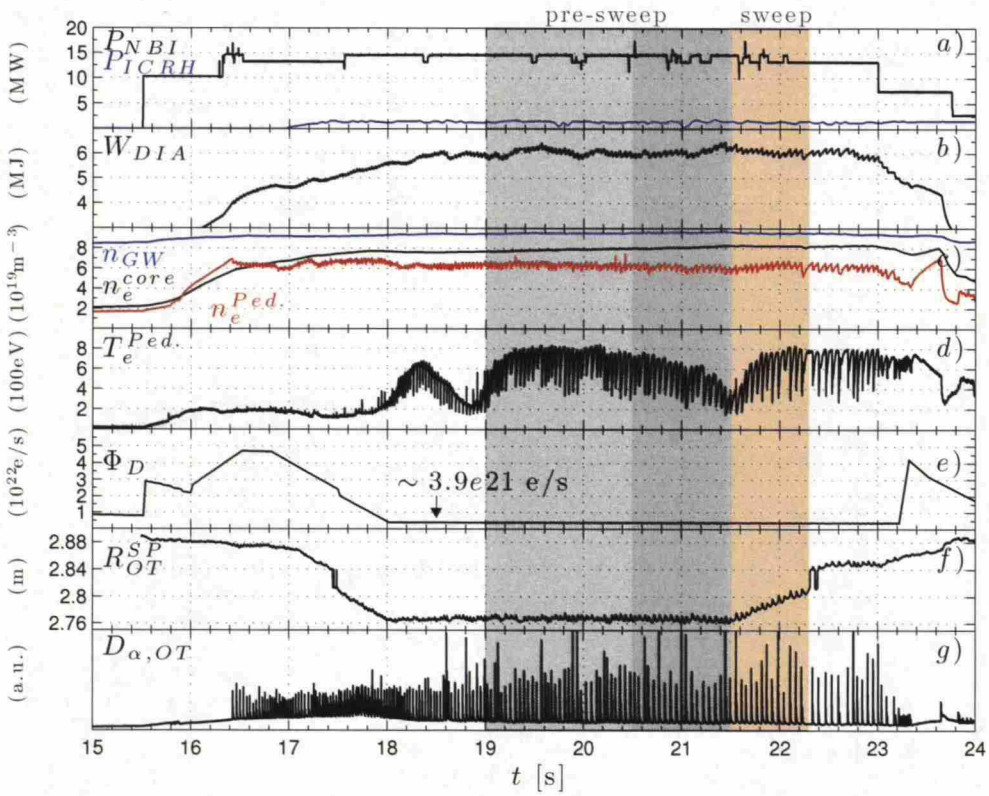

Figure 7: Time-traces: a) Input power: NBI (black), Ion Cyclotron Resonance Radio Frequency Heating (ICRH) (blue); b) Diamagnetic energy; c) Plasma electron density (line average interferometry signal): Greenwald limit (blue), Core (black), Edge (red); d) Pedestal electron temperature (ECE); e) Deuterium fuelling rate (electrons/s); f) Outer strike point R co-ordinate; g) Outer target D_α signal.

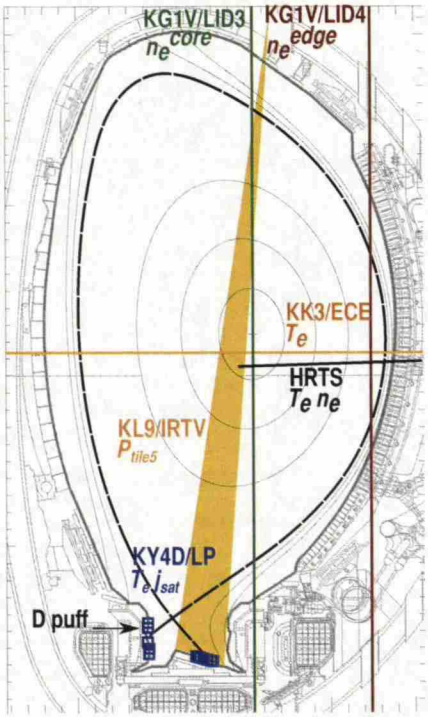

Figure 8: The magnetic equilibrium of JPN 76666 at $t = 20.98$ s as given by the magnetic equilibrium reconstruction (EFIT) with the locations of the diagnostics used in this study: Vertical interferometry (KG1V), Mid-plane fast electron cyclotron emission diagnostic (KK3), Outer mid-plane high resolution Thomson scattering diagnostic (HRTS), Target infra-red camera (KL9), Target Langmuir probes (KY4D) .

energy according to the equations (2) and (4): $\nu^*_{\mathrm{e,\,ped}} \sim 0.35$ and $W_{\mathrm{ped}} \sim 1.8$ MJ. The values for the ion population are obtained by assuming $Z_{\mathrm{effective}} n_{\mathrm{i}} \approx n_{\mathrm{e}}$, $Z_{\mathrm{effective}} \approx 1.6 - 1.9$ and $T_{\mathrm{i}} \approx T_{\mathrm{e}}$. The $Z_{\mathrm{effective}}$ stands for the effective charge state of the plasma. For the volume of the confined plasma, $V_{\mathrm{plasma}} \approx 100\ \mathrm{m}^{-3}$ is assumed. The drop of the pedestal T_{e} signal from 800 eV to 400 eV in the figure 7 during the dark grey time frame is associated with a 1 cm inward radial shift of the outer mid-plane (OMP) separatrix location; therefore, this drop should not be interpreted as a loss of confinement. The time frames in the figure 7 are coloured such that the grey area represent the flat top steady-state plasma before the strike point sweep, the dark grey the part of the discharge during which most of the experimental data compared to the simulations is obtained and the orange the strike point sweep, during which the pre-ELM target *Langmuir probe* (LP) [23] measurements are obtained. The average ELM size in the plasma during the dark grey time frame is around $200 - 300$ kJ ($\sim 10\% - 15\%$ of W_{ped}) interpreted from the temporal evolution of the plasma diamagnetic energy (figure 9a). The diamagnetic energy was used due to its high measurement frequency of about 2500 Hz in this study. It is a topic of ongoing discussion at JET, whether the ELM magnitudes should be interpreted

from the diamagnetic or from the MHD energy data. Accordingly, in future these analysis may be based on some other signal than the diamagnetic one. The amount of power invested in restoring the plasma stored energy between consecutive ELMs is around 3.9 MW (figure 9a). The foot of the outer target D_α rise is used to define the experimental ELM onset, t_{ELM}, in this study (figure 9b).

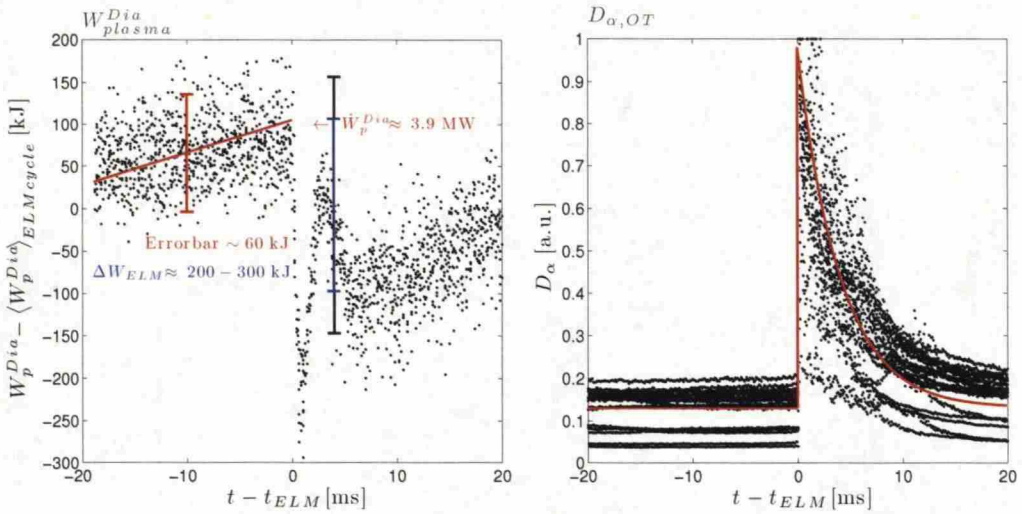

Figure 9: a) The plasma diamagnetic energy over ELMs during $t \in [20.5, 21.5]$ comprising altogether 19 ELMs. The y-axis has been shifted to the average diamagnetic energy during the ELM cycle for each individual ELM. b) The D_α^{OT} signal is used for identifying the ELMs.

Most the used diagnostic locations have been highlighted in the figure 8. The *high resolution Thomson scattering* (HRTS) diagnostic measures the frequency distribution of laser light scattered from the plasma. The distribution contains information about the density and the temperature of the electron population at the scattering location. The HRTS is a snapshot measurement operating with a high time-resolution of about 15 ns [43]. In JET, the HRTS sampling frequency is 20 Hz, and the spatial resolution is 1.5 cm [43]. The Langmuir probes measure the I–V characteristics of the plasma, from which the plasma wall flux, the local electron temperature and the plasma density can be interpreted. The parameters routinely interpreted from the LP measurement data are the electron temperature, T_e, and the ion saturation current, j_{sat}. The Langmuir probe I-V characteristics are interpreted by assuming Maxwellian electron velocity distribution function (EVDF) in front of the probe. The realistic EVDF in the divertor may, however, strongly deviate from Maxwellian [66]. Consequently, under certain conditions, such as in moderate divertor plasma collisionality, T_e interpreted from the LP signals can be overestimated by as much as a factor of five [66]. Accordingly, at least the far SOL,

low T_e values are often not reliably measured with the LPs. The target power flux, q, can be interpreted from the infra-red emission of the target plate measured by an infra-red camera (IRTV) [67]. The interferometry measures the refractive index of the plasma along lines of sight by analysing the phase shift of an electromagnetic beam crossing the plasma [24]. The refractive index provides information about the electron density along the line of sight. The electron cyclotron emission (ECE) diagnostic system measures the electron cyclotron radiation emitted by the electrons accelerating in the magnetic field [24]. This radiation provides information about the local electron temperature.

3.2 Approach to ELM Simulations

The simulations of the ELMy background plasmas in this study are conducted by obtaining first pre-ELM, steady-state EDGE2D/EIRENE solutions. Based on those, ELMs are simulated *ad hoc* by employing short duration enhancements for the cross-field diffusion around the outer mid-plane to transfer a plasma slice from the pedestal to the SOL plasma. This *ad hoc* approach to ELM simulations has been used also in [68] and in [69]. The pre-ELM EDGE2D/EIRENE simulations are benchmarked to the outer mid-plane HRTS measurements of n_e and T_e, and to the target LP and IRTV measurements of T_e, j_{sat} and q. The ELM model is adjusted to mimic the total ELM magnitude and the ratio of the convective ELM losses to the conductive ones by matching these quantities within a factor of two. The simulated ELM losses are compared to the ELM evolution of the plasma diamagnetic energy (figure 9a) and to experimental values based on the results presented in [43]. The ELM dynamics in EDGE2D/EIRENE are further compared to experimental data obtained by the edge interferometry, the edge electron cyclotron emission diagnostics and the outer target IRTV.

The pre-ELM simulations in this study are largely based on the inter-ELM H-mode EDGE2D/EIRENE simulations presented by D. Moulton in [70]. Three plasma densities are simulated in this study: low (outer mid-plane separatrix electron density of $n_{e,\,sep}^{OMP} \sim 2.9 \cdot 10^{19}$ m^{-3}), base ($n_{e,\,sep}^{OMP} \sim 3.6 \cdot 10^{19}$ m^{-3}) and high ($n_{e,\,sep}^{OMP} \sim 4.4 \cdot 10^{19}$ m^{-3}). The base case is similar to the lowest reference case in [70]. In this study, a wider calculation grid was used than in [70] due to the radial depth of the ELM affected area in the core plasma. Associated to this and to the available enhanced OMP T_e profiles, the inter-ELM core and ETB heat conductivities as well as the heat conductivity ETB width were slightly modified to enhance the match with the T_e profile: $\chi_\perp^{core} \approx 0.8$ m^2/s $\rightarrow 1$ m^2/s; $\chi_\perp^{ETB} \approx 0.15$ m^2/s $\rightarrow 0.18$ m^2/s. The calculation grid and the cross-field diffusion

coefficients are presented in the figure 10. Same cross-field diffusion coefficients are assumed for all particle species. The same cross-field heat conductivities have been assumed for electrons and ions as has been done in [68], [69] and [70]. Generally, they are assumed the same because separation is not possible on the basis of the experimental data [68]. Zero cross-field convection has been assumed: $v_{\text{pinch}} = 0$.

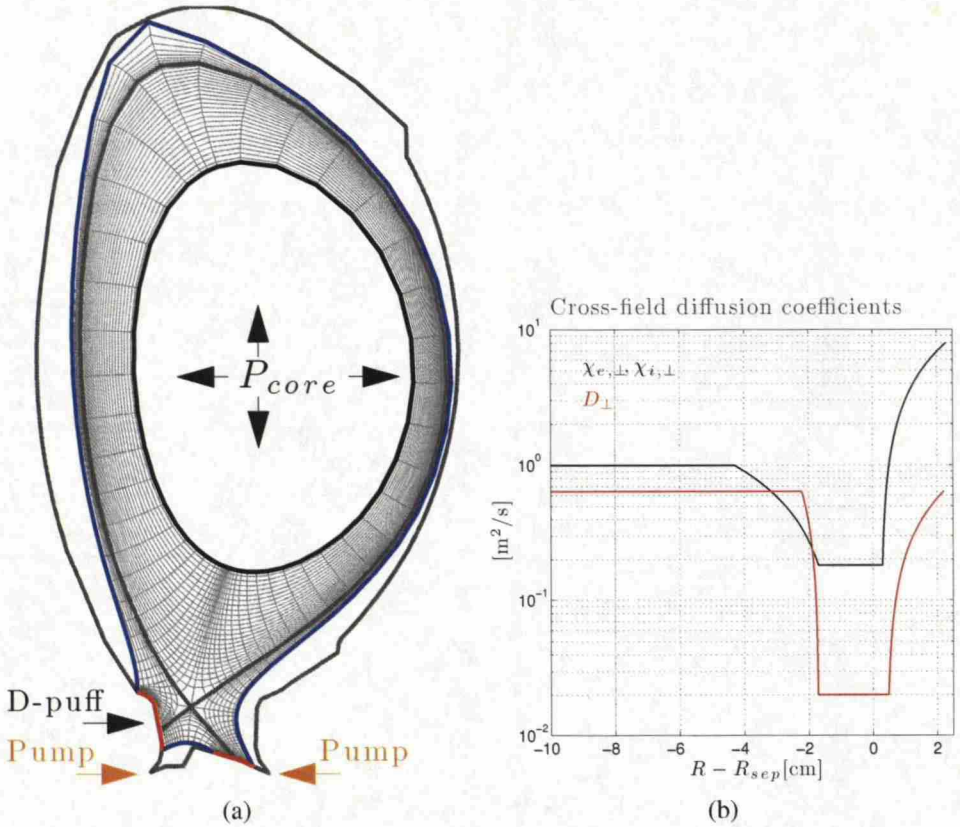

(a) (b)

Figure 10: a) The calculation grid used in the study. The colours represent the different locations for boundary conditions: Main chamber and PFR wall (blue), Targets (red), Core boundary (black), Bulk grid (grey) and Pump (orange). b) The cross-field diffusion coefficients used in the study.

The main boundary conditions used in this study for the EDGE2D/EIRENE simulations are presented below (the colour coding refers to the grid locations of the different boundary conditions as has been illustrated in the figure 10a):

- Deuterium puffing rate [10^{21}e/s]: 3 (Low), 5 (Base), 7 (High)
- Power input [MW]: 10 (Pre-ELM), 14 (Intra-ELM & ELM recovery)
- Flux conservation at core: $\Gamma_{\text{core}}^{\text{in}} = \Gamma_{\text{core}}^{\text{out}}$
- Heat flux limiters: $\alpha_e = \alpha_i = 1.5$
- Density decay length: $\lambda_n^{\text{SOL boundary}} = \lambda_n^{\text{PFR boundary}} = 2.5$ cm

- Temperature drop: $T_i^{\text{wall}} = 0.998 T_i^{\text{SOL boundary}}$, $T_e^{\text{wall}} = 0.9954 T_e^{\text{SOL boundary}}$
- Target plasma flow velocity: $v_{\parallel} = c_s$
- Sheat heat transmission coefficients: $\gamma_e = 4.5$, $\gamma_i = 2.5$
- Carbon chemical sputtering: Roth/Pacher (2003) Flux dependent model [71]; enhancement factor 2; wall flux model: fixed (1e19-Roth, 0-Haasz/Davis [72])
- Carbon physical sputtering [73]: Enhancement factor 1
- Sub-divertor pump: pumping albedo 0.95

The enhancement factor for the carbon chemical sputtering has been widely used for matching the total divertor plasma radiation in the codes as has been done in [70]. The value of two is obtained here by a suggestion by P. Belo. The power input to the core plasma for the pre-ELM EDGE2D/EIRENE simulations is obtained by subtracting the core radiative power and the power invested in restoring the plasma stored energy from the total input power [74]:

$$P_{\text{core}} = P_{\text{in}} - \frac{dW_{\text{plasma}}}{dt} - P_{\text{rad}}^{\text{core}} = (15.7 - 3.9 - 1.8)\ \text{MW} = 10.0\ \text{MW}. \qquad (19)$$

This power is distributed equally to electrons and ions. For the intra-ELM and ELM recovery simulations, the power invested in the plasma stored energy is added to the power input of the simulations leading to 14 MW, which is also distributed equally to electrons and ions.

3.3 Pre-ELM Simulations

The pre-ELM base case matches with the outer mid-plane HRTS profiles (figure 11, the blue line). The density scan ranges OMP separatrix electron densities from $2.9 \cdot 10^{19}$ m^{-3} to $4.4 \cdot 10^{19}$ m^{-3}. The HRTS measurements and the deconvolved profiles are obtained from JPN 79498, which is a companion discharge to JPN 76666 with improved HRTS resolution. The instrument function of the HRTS system is deconvolved through the measurements to obtain the experimental fit [75]. The effect of the deconvolution is to narrow the pedestal of the fitted curve and to lower the otherwise upwards biased separatrix temperatures [75].

The separatrix location in the HRTS data is typically taken from the magnetic equilibrium reconstruction (EFIT). The EFIT OMP separatrix location has, however, typically an uncertainty of about 2 cm, which is comparable to the pedestal gradient length of the JET H-mode discharges (see figure 11). Therefore, the HRTS

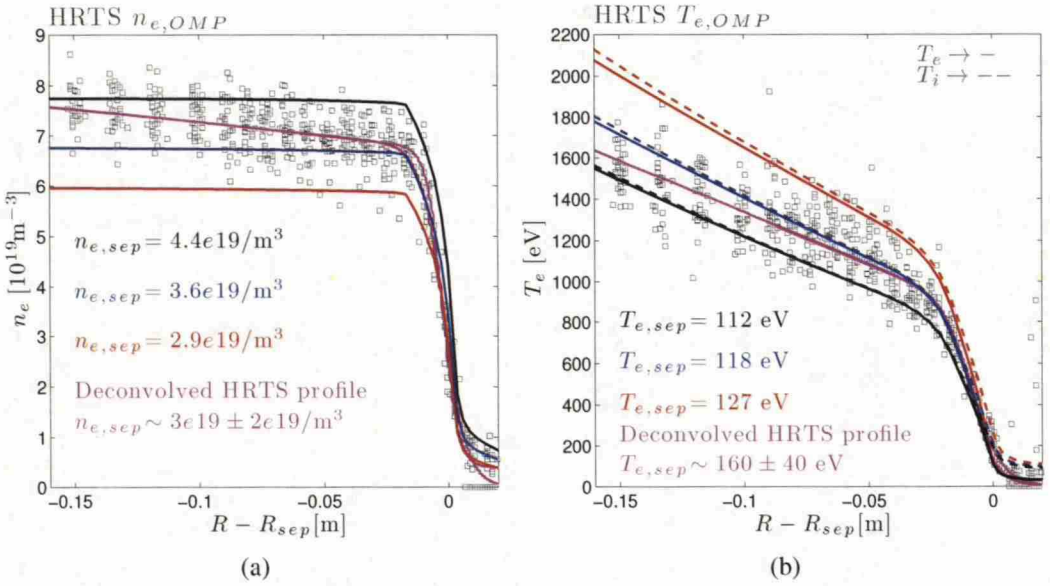

Figure 11: The outer mid-plane HRTS n_e (a) and T_e (b) profiles for the discharge 79498 compared to the pre-ELM profiles of the EDGE2D/EIRENE cases: low (red), base (blue) and high (black). The deconvolved HRTS fit is illustrated by the magenta line.

measurements cannot be used to interpret the separatrix electron density and temperature. Instead, the separatrix values have to be deduced by other means in order to perform an adequate radial shift for the HRTS profiles. In this study, the profiles are shifted to match the separatrix electron temperature obtained by the 2-point model (equation (14)) based on the outer target IRTV heat flux measurements.

The IRTV measures an inter-ELM outer strike point heat flux density of roughly 17.5 ± 2.5 MW/m^2. Assuming twice as high power flux entering the divertor, due to the flux expansion and the volumetric power losses in the divertor, leads to $q_{\text{Entrance}}^{\text{Divertor}} \sim 35 \pm 5$ MW/m^2. Converting this to parallel-**B** with the magnetic pitch angle of about $B_{\text{total}}/B_\theta \sim 25 \pm 10$ at the divertor entrance location gives an estimated parallel-**B** power flux of $q_\parallel^{\text{Max}} \sim 880 \pm 480$ MW/m^2. The 2-point model, together with target electron temperatures of about $T_t^{\text{LP}} \sim 40 \pm 20$ eV and SOL parallel OMP to OT connection lengths of about $L_\parallel^{\text{OMP div.}\rightarrow\text{OT}} = 34$ m, gives an estimated OMP separatrix electron temperature of about $T_{\text{sep}}^{\text{OMP}} \sim 160 \pm 40$ eV. Using this value, the HRTS profiles have been shifted 1.05 cm outwards from the location given by EFIT. Similar shifts have been used in [68], where an adequate outward shift of the order of 1 cm was found by comparing experimental OMP and target profiles to simulation results obtained with the EDGE2D/NIMBUS code package [76].

The pre-ELM base case matches with the outer target (OT) T_e^{LP} and $j_{\text{sat}}^{\text{LP}}$

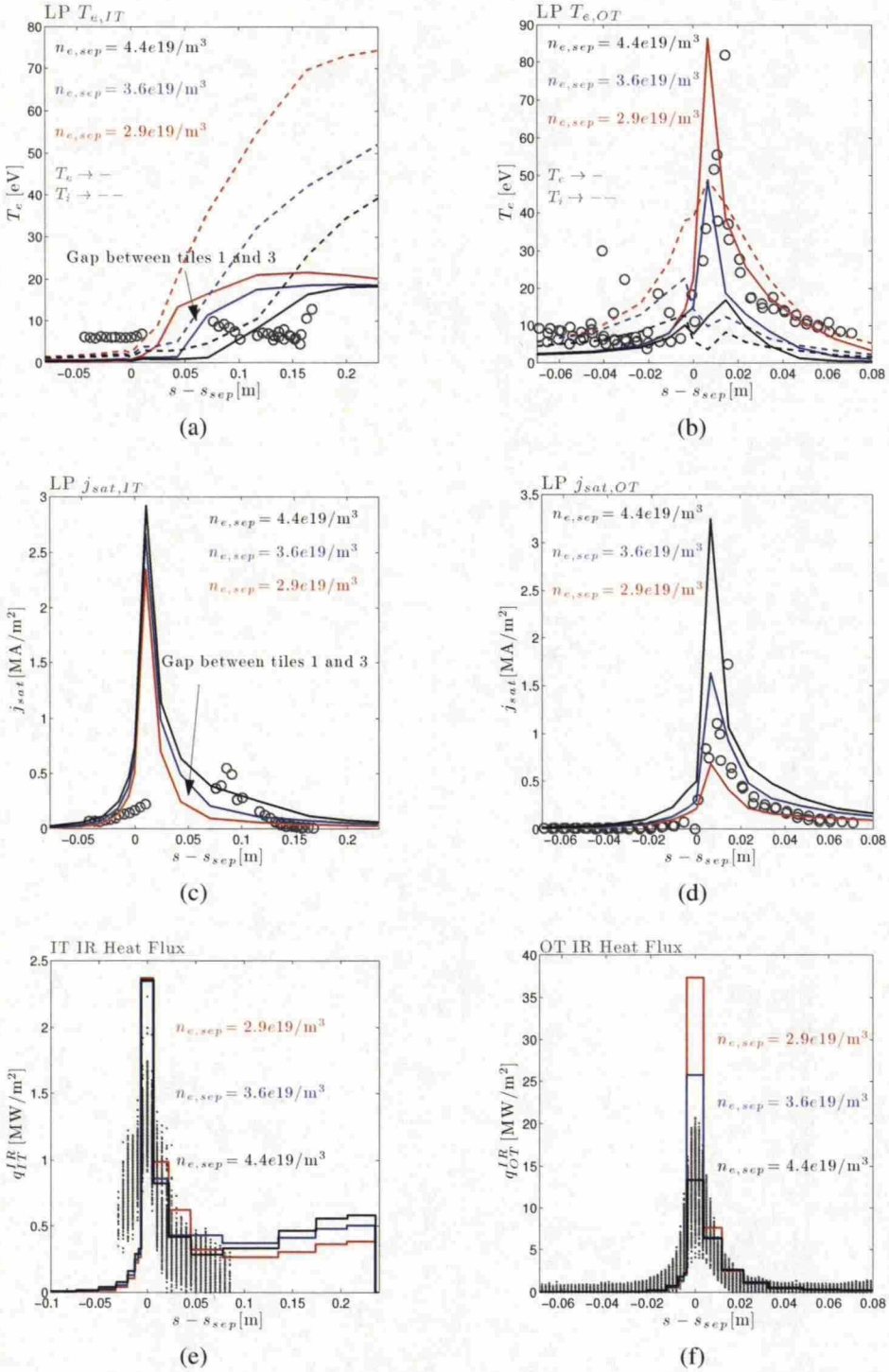

Figure 12: Divertor target measurements compared to the pre-ELM EDGE2D/EIRENE cases: T_e^{LP} a) inner, b) outer; j_{sat}^{LP} c) inner, d) outer; q_{surf}^{IRTV} e) inner, f) outer. The Langmuir Probe measurement are obtained during the strike-point sweep: $t \in [21.5, 22.5]$. The IRTV measurements are obtained for $t \in [20.5, 21.5]$: from 30 ms after an ELM to 1 ms before a subsequent ELM.

measurements (figure 12b and d). The outer target heat flux in the base case is, however, overestimated by 25% compared to the IRTV values (figure 12f). From the equation (8) it is observed that the surface heat flux is determined by T_e, T_i, n_{se}, γ_e, γ_i and B_{total}/B_θ, where the last term is used to convert the parallel-**B** heat flux to the surface heat flux. Not matching the target heat flux indicates that the balance between these terms is not fully reproduced. If EFIT is assumed to provide an accurate magnetic pitch angel at the strike point, the overestimated heat flux is caused by the combination of the target temperatures, the plasma density and the sheath heat transmission coefficients. Although, the used sheath heat transmission coefficients are obtained by separate kinetic simulations based on conditions which may not perfectly resemble the plasma conditions in this study, their effect is not anticipated to provide as high an error bar as 25%. For the target ion temperature, on the other hand, there is no measurement available, thus leaving the degree of match of the ion temperature uncertain. The outer target ion temperatures obtained by EDGE2D/EIRENE are, however, generally very low and, thus a significant overestimation of those is not anticipated. Presumably, although the T_e and j_{sat} are reproduced within the experimental error bars, the slight variation of these variables within the error bars are sufficient to provide an overestimated target heat flux. Lowering the j_{sat} signal of the base case by 25% would, for instance, lower the outer strike point heat flux down to the experimental values while only improving the match with the j_{sat}^{LP}. Accordingly, overestimating the outer strike point heat flux is interpreted to indicate, to first order, that the electron pressure, n_eT_e, at the outer strike point in EDGE2D/EIRENE is overestimated roughly about 20%. Nevertheless, the match is satisfactory for the pre-ELM steady-state plasmas used in the ELMy H-mode simulations in this study, and the 20% pre-ELM deviations are not considered as the greatest sources of uncertainty in the final results. The inner target (IT) strike-point in JPN 76666 is situated between the tiles 1 and 3. Therefore, the Langmuir probe measurements at the inner strike point could not be obtained (figure 12a and c). The inner target strike point heat flux is overestimated compared to the IRTV measurements. Overestimating both the inner and the outer strike point heat fluxes indicates that the parallel-**B** transport may be overestimated in the model compared to the cross-field transport. The IRTV field of view of the inner target in the magnetic configuration of JPN 76666 is, however, very limited and those measurements, especially the intra-ELM ones, are prone to be underestimated.

3.4 ELM Simulations

ELMs are simulated in EDGE2D/EIRENE by multiplying the cross-field diffusion coefficients for a short period on a specified section on the grid. The diffusion coefficients outside the specified section are not changed during the ELM. In this study, the cross-field diffusion coefficients are multiplied on an area spanning radially on $R^{\mathrm{OMP}} - R_{\mathrm{sep}}^{\mathrm{OMP}} \in$ [-8 cm, 0.7 cm] and vertically from -1.05 m below the mid-plane to 1.35 m above it (figure 13).

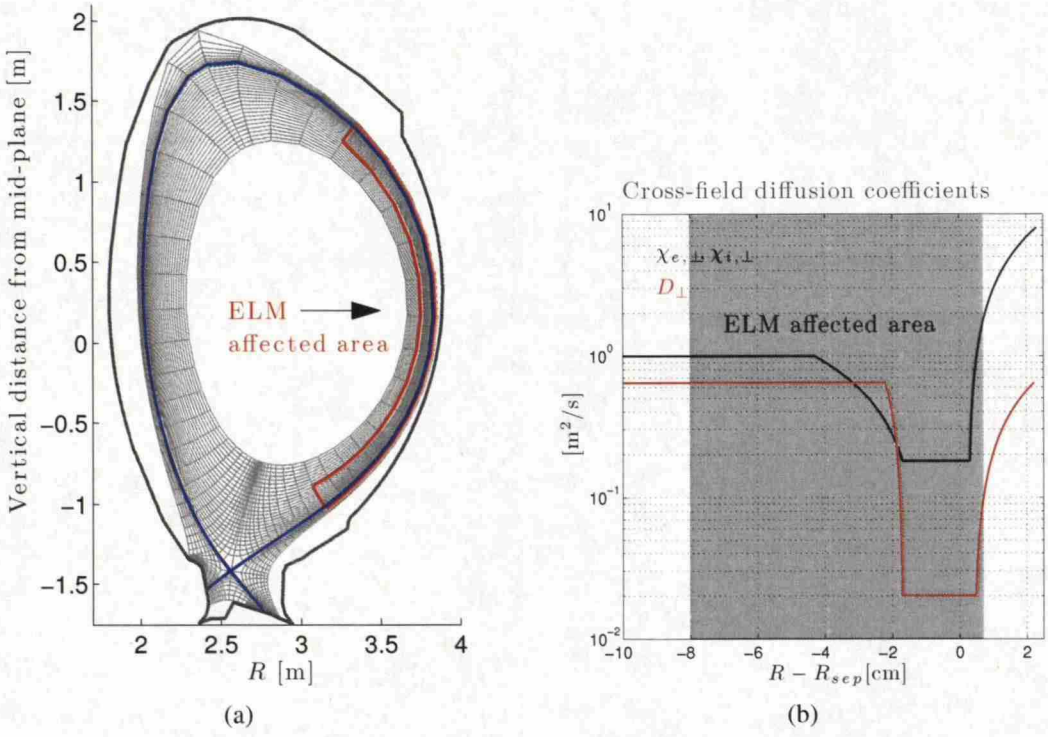

(a) (b)

Figure 13: The ELM affected area in the EDGE2D/EIRENE simulations in this study.

The ELM model is adjusted to mimic the total ELM magnitude as well as the ratio of the convective ELM losses to the conductive ones by matching these quantities within a factor of two. The experimental value for the ELM magnitude is obtained from the time-evolution of the plasma diamagnetic energy (figure 9a). The convective losses are assumed to cause roughly 4 – 6% loss of the pedestal stored energy [43]. The conductive losses are assumed to cause roughly 3 – 10% loss of the pedestal stored energy according to [43], and taking into account the pedestal neoclassical electron collisionality, $\nu^*_{\mathrm{e,\,ped}}$, of JPN 76666 being roughly 0.35.

Three ELM sizes and two durations are considered for the base case density: $\tau_{\mathrm{ELM}} \in \{0.2\ \mathrm{ms},\ 1\ \mathrm{ms}\}$ (table 3). 0.2 ms represents the typical experimentally observed ELM duration interpreted from the duration of the ELM related magnetic

fluctuation phase. 1 ms represents here an upper limit for the ELM duration. The sizes of the simulated ELMs are varied by multiplying the cross-field diffusion multiplier of the medium ELM case (blue in table 3) by 3 and 1/3 to obtain high and low diffusion ELMs (table 3).

Table 3: Input parameters and ELM magnitudes related to the ELM size and duration scan. The last row in the table (grey) presents the obtained experimental values. The colours refer to the figures 14 a–b. τ_{ELM} represents the ELM duration, $M_{D_\perp}$ the $D_\perp$ multiplier, M_{χ_i} the $\chi_i^\perp$ multiplier, M_{χ_e} the $\chi_e^\perp$ multiplier, W_{ELM} the total ELM magnitude (equation (3)), $W_{ELM}^{conv.}$ the convective ELM losses and $W_{ELM}^{cond.}$ the conductive ELM losses.

$\tau_{ELM}[ms]$	$M_{D_\perp}$	M_{χ_i}	M_{χ_e}	W_{ELM} [kJ]	$W_{ELM}^{conv.}$ [kJ]	$W_{ELM}^{cond.}$ [kJ]	$W_{ELM}^{conv.}/W_{ELM}^{cond.}$
1	900	75	25	232	113	141	0.80
1	300	75	25	213	98	132	0.74
1	100	75	25	175	67	119	0.56
0.2	9000	1500	500	180	70	126	0.56
0.2	3000	1500	500	175	67	123	0.55
0.2	1000	1500	500	162	58	117	0.50
Experim.				200 – 300	$\sim 110 \pm 30$	$\sim 120 \pm 60$	$\sim 0.9 \pm 0.7$

The total ELM magnitudes in the medium and high diffusion 1 ms ELM cases are comparable to the lower end of the experimental ELM magnitude range (table 3). The 0.2 ms ELMs are too short for a sufficient power transport across the separatrix to occur to match the ELM size. The ratio of the convective losses to the conductive ones is comparable to the middle experimental range in the high and medium diffusion 1 ms EDGE2D/EIRENE cases (table 3). The 0.2 ms ELMs are too short for sufficient diffusive ELM losses to occur to match the convective losses. Therefore, the total ELM magnitude in the 0.2 ms ELMs is underestimated, and the convective-conductive ratio is biased towards the lower end of the wide experimental range.

The radial shape of the ELM losses cannot be matched with such a simplistic purely diffusive ELM model, as has been used in this study, in which radial variation are not included into the intra-ELM cross-field diffusion enhancement. The radial distribution of the convective and conductive ELM losses are compared to experimental observations in the figure 14. These experimental observations are presented in [43] and obtained on discharges with pedestal collisionalities of $\nu_e^* \sim 0.15$ and $\nu_e^* \sim 0.6$. The constant ELM multiplier on the specified section on the grid imposes a radially flat profile for the convective losses on the ELM affected area (figure 14). The greatest conductive ELM losses are imposed on the core boundary side of the ELM affected area (figure 14). In the experiment, on the other hand, the greatest losses occur around the pedestal top location. Furthermore, the shape of the ETB is not smoothened in EDGE2D/EIRENE during the intra-ELM phase. This leads to plasma accumulation around the location of the separatrix, which can be seen

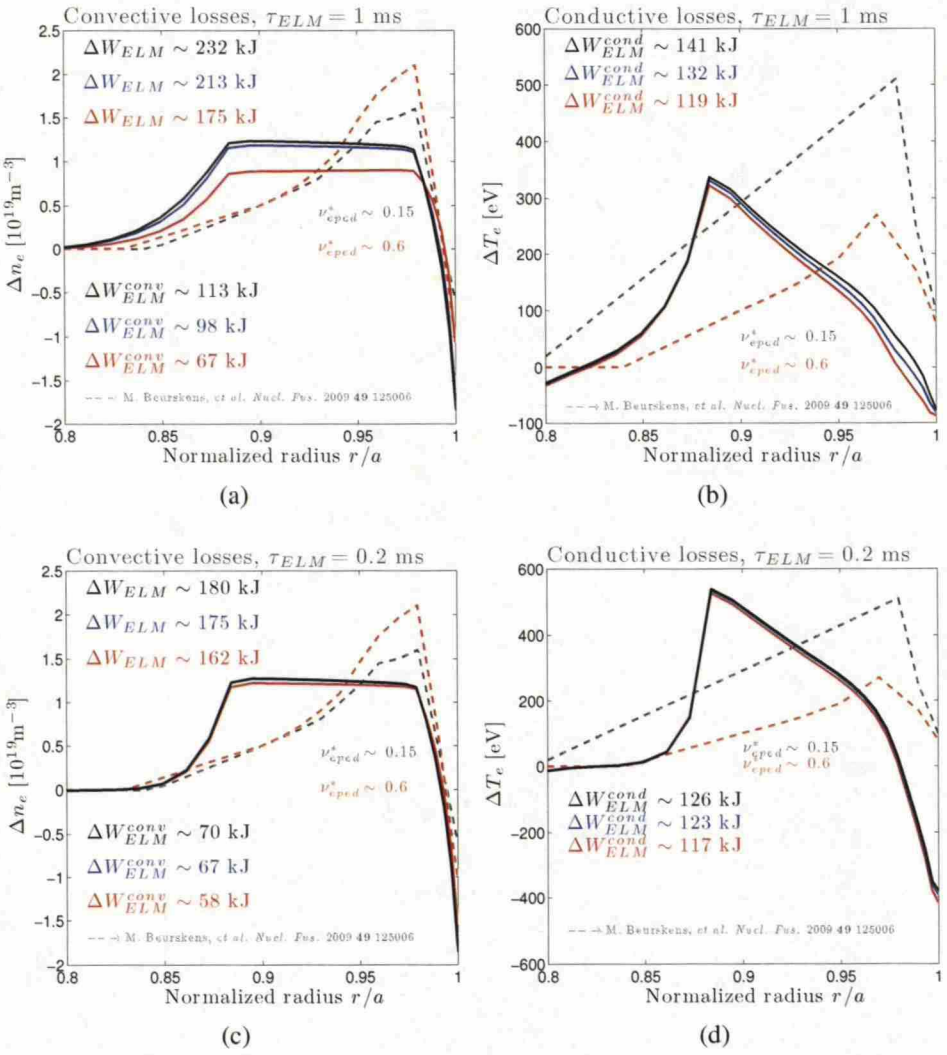

Figure 14: The convective and conductive ELM magnitudes compared to the measured profiles for discharges with pedestal collisionality $\nu^* \sim 0.15$ (dashed grey) and $\nu^* \sim 0.6$ (dashed orange) obtained from [43]. The colours refer to the table 3. The total, the convective and the conductive ELM magnitudes obtained in the simulations are written on the figures.

especially in the radial distribution of the conductive losses (figure 14). Using convective ELMs by imposing *ad hoc* v_{pinch} instead of $D_\perp$ would probably enable a better match with the radial distribution. Nevertheless, from the figure 14 it can be observed that the area below the curves are comparable to the experimental ones. Together with comparable ELM loss magnitudes to the experimental ones (table 3), this indicates that the chosen multiplier values, as well as the chosen ELM affected area, lead to a satisfactory match with the experimental ELM losses.

Within the spanned range in the $D_\perp$ multiplier, the ELM losses do not vary significantly. This indicates that the used multiplier values are close to the saturation point, i.e. they provide a flat intra-ELM density profile, and much additional ELM

size cannot be gained by further increasing the $D_\perp$ multiplier. This issue could also be overcome by imposing intra-ELM v_{pinch} instead of enhanced $D_\perp$.

From now on, the comparisons of the ELM dynamics between the simulations and the experimental estimates will be done only for the medium $D_\perp$ multiplier ELMs of 1 and 0.2 ms.

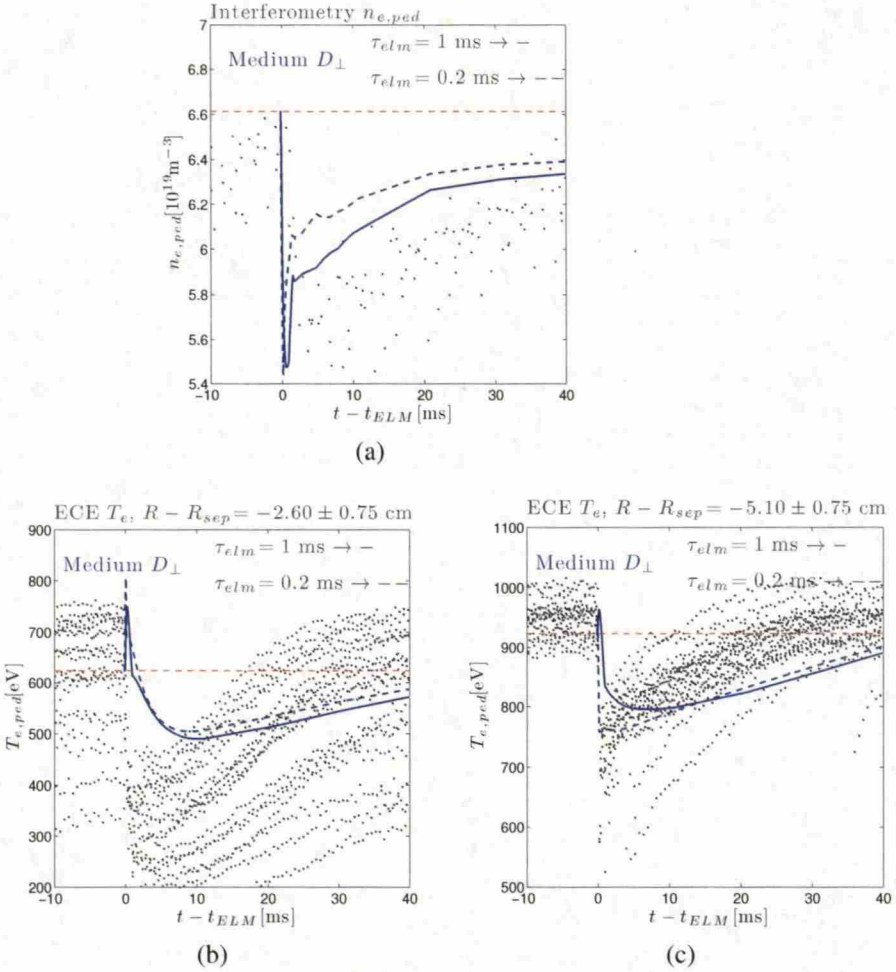

Figure 15: The outer mid-plane dynamics of the medium $D_\perp$ multiplier ELMs of 0.2 ms and 1 ms compared to the ECE and the edge interferometry measurements of T_e and n_e. The T_e values are compared at two radial locations: $R - R_{\text{sep}}^{\text{OMP}} \approx -2.6$ cm (pedestal) and -5.1 cm. The dashed red-lines represent the pre-ELM values of the simulated EDGE2D/EIRENE cases.

Comparing the outer mid-plane pedestal dynamics of n_e and T_e to the edge interferometry and the electron cyclotron emission measurements demonstrates that the outer mid-plane n_e drop and the T_e drop at $R - R_{\text{sep}}^{\text{OMP}} \approx -5.1$ cm are reproduced (figure 15). The ELM recovery time of the pedestal T_e is overestimated by a factor of two during the first $10 - 20$ ms after the ELM onset (figure 15). It is also observed that the near separatrix T_e at $R - R_{\text{sep}}^{\text{OMP}} \approx -2.6$ cm drops much slower after the ELM

onset than the experimental signal. This relates also to the radial distribution of the ELM losses not being matched to the experimental estimations (figure 14). The degree of match could presumably be enhanced by imposing convective rather than diffusive model for the ELMs.

Not matching the pedestal recovery dynamics stems presumably from the quasi-time-dependent approach taken in this study. ELMs are simulated as single events on a steady-state pre-ELM background plasma, and the cross-field coefficients adjusted to match the pre-ELM profiles on a steady-state approach may not match the cross-field transport during the ELM recovery phase. This may stem from the balance between diffusive and convective transport. The time-evolving background plasma may be more sensitive to the ratio of these two, whereas a satisfactory steady-state solution can be obtained by employing only the cross-field diffusion.

In simulating the SOL of an ELMy H-mode plasma, the zeroth order terms to match are the SOL input power, i.e. power crossing the separatrix, and the SOL density. The detailed time-evolution of these parameters through an ELM cycle is, however, beyond the diagnostic capability of the available instruments. Therefore, the degree of match have to be interpreted from the time-evolution of the pedestal T_e and n_e, as well as from the match of the simulated ELM magnitudes with the experimental values. These were compared to experimental measurements in the table 3 and in the figure 15. It was observed that, taking the simplicity of the used *ad hoc* approach, these quantities are encouragingly comparable to the experimental values. Further enhancement to the match of the pedestal and, consequently, the separatrix T_e values could presumably be obtained by using a convective approach to the ELM simulations.

3.5 ELM Energy SOL Transport

The experimental values for the outer target ELM power deposition are obtained by multiplying the outer target tile 5 power deposition, measured by the IRTV, with an enhancement factor taking into account the estimated power deposition on the tiles 6 – 8 (figure 5b). For the inner target, double of the ELM power deposited at the outer target is assumed according to [77].

A mid-plane power decay length of $\lambda_{ELM} \approx 3.5$ cm has been measured for medium sized ELMs ($E_{ELM}^{ped}/E_{ped} \approx 0.12$) [42], such as the ones in JPN 76666. Assuming that all the ELM power is deposited through convection and conduction, this gives estimates for the fractions of the ELM energy reaching the main chamber wall, f_{wall}, the strike-point target tiles 3 and 5, $f_{\#3+\#5}$, and the far SOL target tiles,

$f_{\text{far SOL target}}$ [78]:

$$
\begin{aligned}
f_{\text{wall}} &= \frac{E_{\text{ELM}}^{\text{wall}}}{E_{\text{ELM}}^{\text{ped}}} = \exp(-\Delta_{\text{wall}}^{\text{ELM}}/\lambda_{\text{ELM}}) = \exp(-(\Delta_{\text{wall}}+\Delta_{\text{ELM}})/\lambda_{\text{ELM}}) \\
f_{\text{far SOL target}} &= \frac{E_{\text{ELM}}^{\text{far SOL target}}}{E_{\text{ELM}}^{\text{ped}}} = \exp(-(\Delta_{\text{IR}}+\Delta_{\text{ELM}})/\lambda_{\text{ELM}}) - f_{\text{wall}} \\
f_{\#3+\#5} &= \frac{E_{\text{ELM}}^{\text{IR}}}{E_{\text{ELM}}^{\text{ped}}} = 1 - f_{\text{wall}} - f_{\text{far SOL target}},
\end{aligned}
\tag{20}
$$

where Δ_{wall} represents the inter-ELM distance from the outer mid-plane separatrix to the outer limiter, Δ_{IR} the inter-ELM radial outer mid-plane SOL width corresponding to the SOL plasma terminating at the tiles 3 and 5 and Δ_{ELM} the uncertainty of these values caused by ELMs. The values for these parameters in this study are $\Delta_{\text{wall}} \sim 6$ cm, $\Delta_{\text{IR}} \sim 2$ cm and $\Delta_{\text{ELM}} = \Delta_{\text{ped}}/2 \sim 1.5$ cm. The latter relationship is taken from [78], where the Δ_{ped} represents the radial width of the pedestal at the outer mid-plane. The used Δ_{wall} value is the average outer separatrix to wall gap given by EFIT on JPN 76666 during 20.5 – 21.5 s (dark grey time frame in the figure 7). Using these numbers the fractions become: $f_{\text{wall}} \sim 0.12$, $f_{\#3+\#5} \sim 0.63$ and $f_{\text{far SOL target}} \sim 0.25$. These fractions determine the estimated target power depositions of ELMs used here:

$$
\begin{aligned}
P_{\text{ELM, OT}}^{\text{IRTV}} &= \frac{f_{\#3+\#5} + f_{\text{far SOL target}}}{f_{\#3+\#5}} P_{\text{ELM, tile 5}}^{\text{IRTV}} \approx 1.4 P_{\text{ELM, tile 5}}^{\text{IRTV}}, \\
P_{\text{ELM, IT}} &\approx 2 P_{\text{ELM, OT}}^{\text{IRTV}} \approx 2.8 P_{\text{ELM, tile 5}}^{\text{IRTV}},
\end{aligned}
\tag{21}
$$

where $P_{\text{ELM, tile 5}}^{\text{IRTV}}$ represents the tile 5 value measured by IRTV. These corrections are presumably strongly related to the ELM filamentary transport, the deposition time-scale of which is foreseen to be comparable to the ion sound-speed: $\sim< 1$ ms. Therefore, the corrections are used as such only for the first millisecond after the ELM onset. After the first millisecond following the ELM onset, the inner target values are not considered and the outer target correction is assumed to decay to 1 with a time constant of 1 ms.

The total energy deposited at the targets during the medium $D_\perp$ multiplier ELMs is matched with the experimental values (figure 16). The in/out asymmetry is, however, inverted compared to the typical experimental observations in JET. The asymmetry in EDGE2D/EIRENE is $E_{\text{in}}^{\text{ELM}}/E_{\text{out}}^{\text{ELM}} \approx 0.5$, whereas usually in JET normal field direction discharges $E_{\text{in}}^{\text{ELM}}/E_{\text{out}}^{\text{ELM}} \approx 2$ is observed [77]. This indicates that there are physical phenomena driving strong intra-ELM heat flow towards the inner

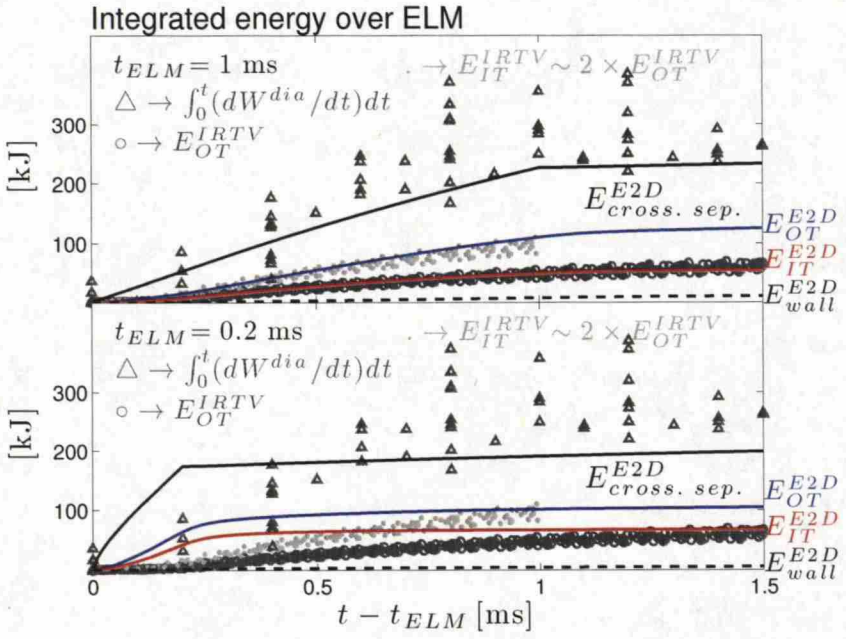

Figure 16: The ELM energy dynamics compared to the experimental measurements: Integrated change of the plasma diamagnetic energy (triangles); Integrated energy deposited at the outer target (circles); Integrated energy estimated to be deposited at the inner target (dots). EDGE2D/EIRENE medium $D_\perp$ multiplier cases of 1 ms (upper), and 0.2 ms (lower): energy crossed separatrix (black solid line); energy deposited at the outer target (blue solid line); energy deposited at the inner target (red solid line); energy deposited at the main chamber wall (black dashed line). Inner target power deposition of double the outer target value is assumed.

target in the normal field direction discharges, and these phenomena are not included in EDGE2D/EIRENE. In EDGE2D/EIRENE the asymmetry is presumably dominantly driven by the target connection length from the source location. In reality, on the other hand, phenomena such as the induced toroidal loop voltage associated with a suppression of the pedestal bootstrap current (see [12] for definition) due to flattening of the ETB may drive considerable ion currents to the inner target [79].

The dynamics of the power crossing the separatrix in the 1 ms ELM case are similar to the dynamics of the change of the diamagnetic energy in the experiment (figure 16). This does not, however, indicate that the 1 ms ELM would provide a match to the experimental value of the power crossing the separatrix during an ELM: $P_{\mathrm{sep}}^{\mathrm{ELM}}$. Instead, the rate of energy output from the entire plasma is matched. The 1 ms ELM presumably imposes a small enough $P_{\mathrm{sep}}^{\mathrm{ELM}}$ to limit the energy output from the plasma to match the total power exhaust rate, although the simulated power transport in the SOL in EDGE2D/EIRENE is otherwise too rapid. The pedestal T_{e} signal suggest that the 0.2 ms ELM is plausible to impose a $P_{\mathrm{sep}}^{\mathrm{ELM}}$ closer to the experimental values (figure 17), whereas the target energy deposition dynamics in

the 0.2 ms ELM case are too rapid (figure 16). Therefore, due to the inability of the EDGE2D/EIRENE to model the kinetic transport of the ELM filament in the SOL, the 1 ms ELM leads to a better match to the total summed energy exhaust dynamics.

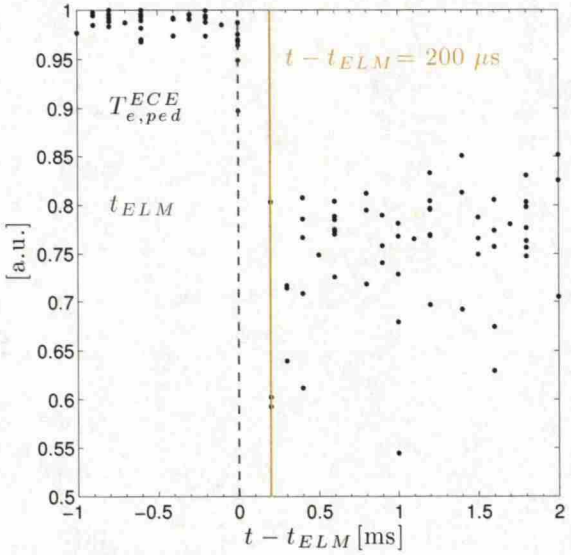

Figure 17: Time-evolution of pedestal ECE T_e for ELMs between 20.5 and 21.5 seconds. Values normalized to 1 for investigating the dynamics. The most significant pedestal T_e drop occurs within the first 200 μs after the ELM onset.

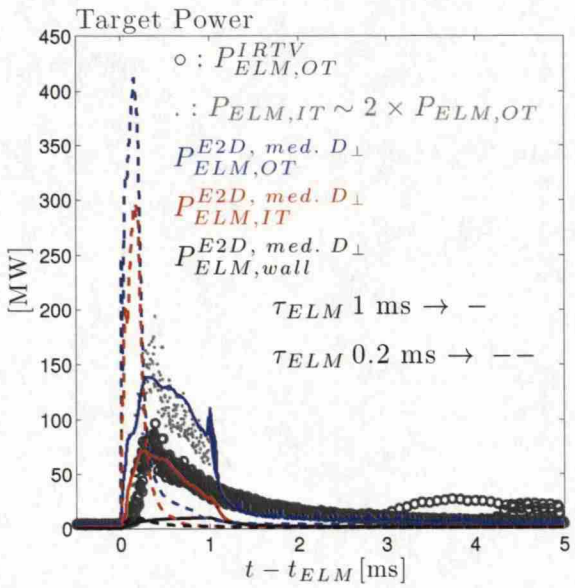

Figure 18: Power deposition: Experimental: Outer target (circles), Inner target (dots); EDGE2D/EIRENE medium $D_\perp$ multiplier, solid 1 ms, dashed 0.2 ms: Outer target (blue), Inner target (red), Main chamber wall (black). Experimental inner target power deposition of double the outer target value is assumed.

The total target power deposition is reproduced in the 1 ms ELM case, although the in/out asymmetry is inverted. The 0.2 ms ELM leads to a factor of three overestimated total peak power deposition and a factor of five underestimated duration of the ELM power deposition at the targets (figure 18). Due to the extremely rapid power transport in the SOL, the 0.2 ms ELM case imposes very high temporal target power fluxes, which would exceed the engineering limits of the material. This can, however, be considered as an unphysical artefact of the simulation code caused by overestimated parallel-**B** power transport in the code. The realistic time-scales are anticipated to be roughly a factor of five longer as is observed from the IRTV data in the figure 18. Although the total target power depositions in the 1 ms ELM case are roughly matched, the onset of the ELM deposition at the targets begins sooner in EDGE2D/EIRENE than in the IRTV measurement data (figure 18). This also suggests too rapid energy transport in the SOL.

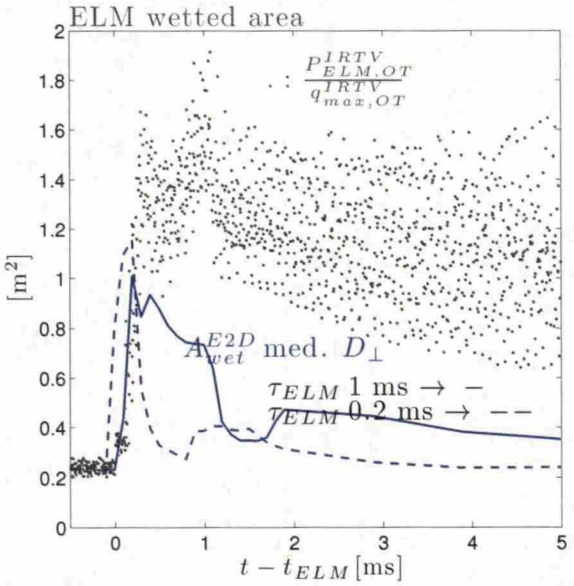

Figure 19: Outer target ELM wetted area: $P^{\text{IRTV}}_{\text{ELM, OT}}/q^{\text{IRTV}}_{\text{max, OT}}$ (dots); medium $D_\perp$ multiplier EDGE2D/EIRENE cases: 1 ms (solid line), 0.2 ms (dashed line).

The outer target plasma wetted area is matched within a factor of 1.5 during the intra-ELM phase, and during the ELM recovery phase the plasma wetted area is underestimated by a factor of 3 compared to the experimental values based on the IRTV measurements (figure 19). The results are similar to the ones obtained with the integrated code suite JINTRAC [80] on a low triangularity ILW reference discharge 73569 documented in [81]. In the JINTRAC study in [81], the ELM wetted area was also matched within a factor of 1.5, and the area showed more rapid decay in the model than in the experiment leading to underestimated ELM

wetted area right after the ELM deposition at the target. In JINTRAC model there occurred, however, a second peak in the wetted area roughly 3 – 4 ms after the ELM onset. This peak is not observed in the EDGE2D/EIRENE simulations here. In JPN 73569 the experimental ELM wetted area decayed back to pre-ELM values within 5 ms after the ELM onset [81], whereas the obtained experimental estimates for JPN 76666 suggest elevated ELM wetted are until 10 – 15 ms after the ELM onset.

Underestimating the ELM recovery wetted area indicates that during the recovery phase the ratio of the parallel-**B** power transport to the cross-field transport is overestimated leading to highly localized power depositions at the strike points. The plasma wetted area in the EDGE2D/EIRENE drops significantly once the ELM enhanced OMP cross-field transport stops. This drop is much more rapid than the slow decay of the plasma wetted area observed in the experiment. Accordingly, the cross-field transport coefficients of the recovery phase are presumably not sufficient to provide as significant cross-field transport as observed in the experiment. A convective component in the cross-field transport could probably amend this issue.

The experimental estimates calculated here take into account the power deposition at the far SOL targets, whereas the calculation grid does not extend far beyond the outer edge of the tile 5: $R - R_{\mathrm{sep}}^{\mathrm{OMP}} \approx 2$ cm flux surface (figure 8b). Accordingly, the power deposited at the tiles 6 – 8 in the EDGE2D/EIRENE contributes to the main chamber power load, rather than to the target power load. To take this discrepancy into account, the main chamber power deposition over the ELM is added to the figures 16 and 18. It is observed that the main chamber power deposition in the EDGE2D/EIRENE cases is indeed negligible compared to the target power deposition; therefore, the error caused by not including the tile 6 - 8 contributions to the target power deposition in the EDGE2D/EIRENE simulations is negligible. Essentially, the plasma wetted areas simulated by EDGE2D/EIRENE are small enough to guarantee that most of the power deposition in the model occurs on the target regions spanned by the calculation grid. Matching the plasma wetted areas in the simulations would actually provide further challenges in the models as the calculation grid does not extend over the far SOL targets, while a non-negligible plasma-wall interaction is anticipated there due to the significant radial transport of the ELM filaments. This issue relates to the general simulation challenges faced by the high triangularity plasmas, which generally contain very narrow scrape-off layers invalidating the main chamber boundary conditions used in the codes.

The parallel-**B** ELM power transport in the SOL is highly overestimated in EDGE2D/EIRENE compared to the IRTV measurements (figures 20a and b). The outer target power deposition begins immediately after the ELM onset in

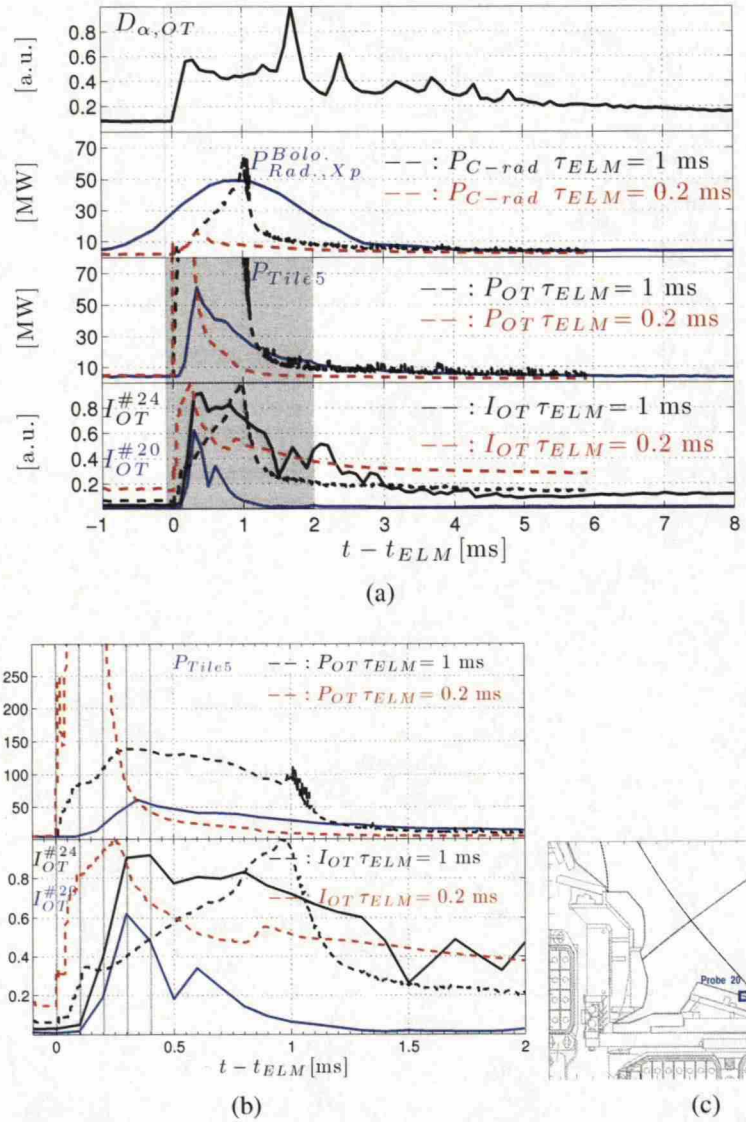

Figure 20: a) Time traces for a representative ELM: D_{α}^{OT}, divertor radiation $P_{Rad.,\,Xp}^{Bolometer/KB5}$ (blue solid line), $P_{Tile\,5}^{IRTV}$ (blue solid line), normalized I_{sat} at two location at the outer target. b) Close-up from the shadowed area in the figure a. c) The locations of the LPs from which the I_{sat} signals are obtained. The dashed lines represent the medium $D_{\perp}$ multiplier EDGE2D/EIRENE ELM cases: black 1 ms, red 0.2 ms. The radiation caused by carbon in the simulations is compared to the bolometer signal. The effect of the background deuterium to the radiation in EDGE2D/EIRENE during ELMs is only around 1 – 2 MW. The bolometer signal has been shifted 2.56 ms backwards in time to take into account the time delay in the measurement instruments.

EDGE2D/EIRENE and obtains the half maximum value around $t - t_{ELM} \approx 50 - 90\ \mu$s, whereas the experimental IRTV signal begins to rise 100 μs after the ELM onset and obtains the half maximum value around $t - t_{ELM} \approx 250\ \mu$s. The IRTV time scales are comparable to the ion sound-speed power transport from the OMP to the outer target. As the LP saturation current signals show similar dy-

namics, this leads to the conclusion that most of the ELM power is transferred to the targets via ions in a time scale comparable to the ion sound speed. Similar dynamics have been observed in kinetic particle-in-cell (PIC) simulations in [82] and in experiments [79]. In EDGE2D/EIRENE, on the other hand, the contribution of the electron channel to the target ELM power deposition exceeds the contribution of the ion channel significantly (figure 21). In the EDGE2D/EIRENE simulations 2/3 of the power to the targets is carried by the electron channel. From the figure 21 it is observed that the overestimation of the electron contribution is the dominant effect leading to the overestimated power transport in EDGE2D/EIRENE. As the electron transit time in the SOL is very short, $\tau_{e,\parallel} \approx L_\parallel / c_e \sim 3\ \mu$s, the ELM pedestal power deposited on the electron channel is transported extremely rapidly giving instant ELM power deposition at the targets. Therefore, overestimating the electron contribution leads to underestimated transport time scales. Furthermore, it is observed from the figure 21 that the time scales of the ion power transport are encouragingly close to the IRTV data (red and grey lines). Therefore, inverting the electron-ion balance in the model would presumably lead to power transport time scales comparable to the experimental observations.

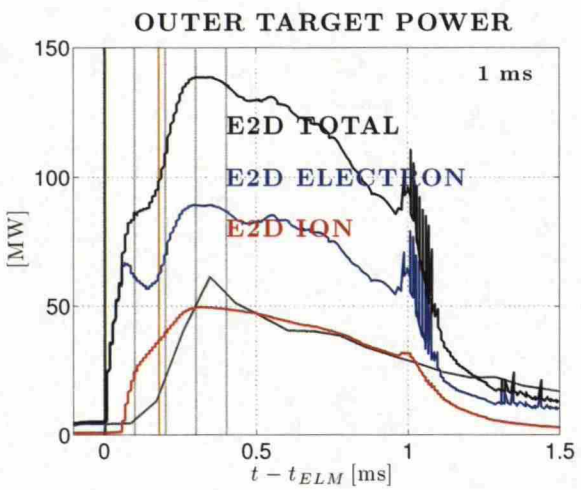

Figure 21: Contributions of electron and ion channels to the outer target power deposition in the medium $D_\perp$ 1 ms ELM. The target power deposition is highly dominated by the electron channel, which transfers 2/3 of the energy reaching the outer target. The grey line represents the tile 5 power deposition as measured by IRTV. The green-line represent the estimated electron transit time $\sim 3\ \mu$s and the orange line the estimated ion transit time $\sim 180\ \mu$s.

According to the PIC simulations in [82], the ELM target deposition dynamics constitute of combination of electrons arriving first nearly collisionlessly to the solid surface causing sheath-limited conditions with increased target electron temperature, and ions arriving later at the time scales comparable to the ion sound

speed transporting most of the ELM energy to the targets. The SOL density remains elevated of the order of roughly 5 ms after the ELM onset (observe the saturation current signal of the probe 24 in the figure 20a). Therefore, after the ions reach the target plates, the SOL is anticipated to evolve towards high recycling conditions, thus rapidly lowering the target temperatures. Therefore, the ELMs are anticipated to lead to a sequence of increased target temperature followed by increased target density, thus imposing a cycle through the three characterized SOL plasma regimes: conduction limited (pre-ELM), sheath-limited (intra-ELM) and high-recycling/detached (ELM recovery). Comparing the target power and flux signals in the figure 20b, these processes are qualitatively reproduced by EDGE2D/EIRENE, but the power transport time scales are too rapid. In the EDGE2D/EIRENE simulations, the target power rises first and the SOL becomes sheath-limited ($\nu^* \sim 2$). Later, the density at the target begins to rise leading to high recycling SOL, with target density remaining elevated of the order of 5 – 10 ms after the ELM onset (see figure 20a: saturation current). The overestimation of the electron contribution to the parallel power transport is anticipated to lead to overestimated intra-ELM target electron temperature; therefore, the detailed time-evolution of the target density and electron and ion temperatures are not necessarily reproduced by EDGE2D/EIRENE.

The overestimated electron contribution stems partially from the assumption of constant sheath-heat transmission coefficients. These kinetic corrections are derived assuming inter-ELM steady-state plasma conditions. Therefore, employing them in simulations of such kinetic phenomena as ELMs is prone to provide extensive error bars to the mutual balance between the electron and the ion channels. Essentially, the ELMs lead to a strong supra-thermal electron burst at the target plates, which increases the sheath-potential, and thus buffers the electron power reaching the targets. This dynamical evolution of the sheath is not included in the multi-fluid codes. In other word, the fluid codes do not take into account the kinetic evolution of the sheath, which may have a significant effect to the intra-ELM physical phenomena, such as target sputtering and impurity transport, in the SOL. Therefore, the assumption of constant, negligibly thin sheath may be considered as one of the most severe deficiencies of the ELM model used in this study. Therefore, the subsequent studies should employ time-evolving sheath heat transmission coefficients, the values of which are obtained from kinetic PIC simulations as has been documented in [83].

The 1 ms medium $D_\perp$ multiplier ELM gives time-evolving plasma radiation comparable to the KB5 bolometer measurement (figure 20a). The simulation lines shown in the plot represents the radiation caused by carbon in the model. The

radiated power caused by background deuterium is below 2 MW throughout the ELM cycle in both 1 and 0.2 ms cases and, therefore, of trace level compared to the carbon radiation. The 0.2 ms ELM is too short for sufficient carbon erosion at the target plates to occur to match the time-evolution of the divertor radiation.

The experimental divertor radiation is comparable to the experimental outer target deposited energy (figure 20a). The divertor radiation begins to rise after the

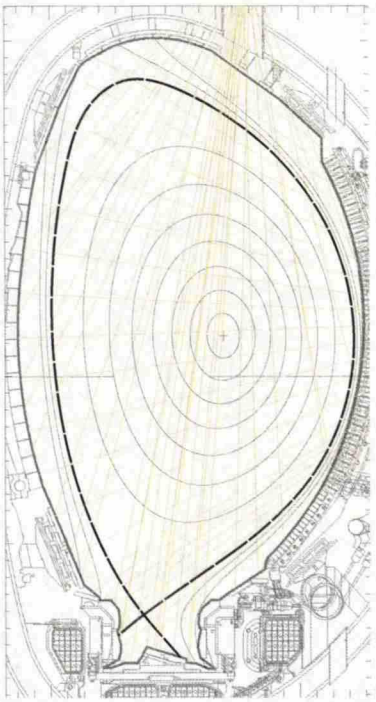

Figure 22: The lines of sight of the KB5 bolometer.

ELM onset and stays elevated during the first 2 – 3 ms. It should be noted, however, that the bolometer system suffers from a poor time resolution as the filter sampling rate is only 200 Hz. Therefore, the obtained measurement data can be seen only as an approximative estimate of the actual radiation dynamics. The estimated divertor radiation illustrated in the figure 20a is obtained by subtracting the estimated core radiative power from the total radiative power measured by the KB5 bolometer. The signal has been shifted 2.56 ms backwards in time to take into account the measurement delay associated with the instrument. The KB5 bolometer observes the divertor through the main plasma (figure 22). To obtain measurements of the divertor radiation with lines of sight not looking through the main plasma, line integrated signals from the divertor bolometer system KB3 are illustrated for comparison purposes in the figure 23. The KB3 signal is also shifted by 2.56 ms. It is observed that the divertor radiation is indeed considerably elevated during the first 2 ms after the ELM onset.

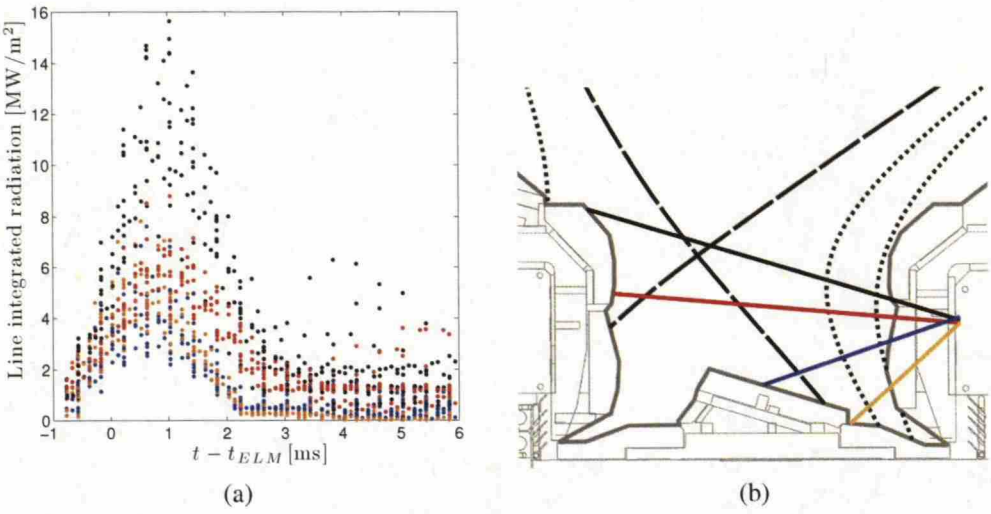

(a) (b)

Figure 23: Line integrated radiation signals from the divertor KB3 bolometer system. It is observed that the divertor radiation rises considerably during the ELM onset. The signal has been shifted 2.56 ms backwards in time to take into account the delay associated with the measurement instruments.

3.6 Summary of the ELM Simulations

In simulating the erosion of divertor targets, and the subsequent transport of the released impurities, the most important background plasma parameters to match are the divertor plasma density and the temperatures of electrons and ions. Time-evolving measurements of these parameters over an ELM cycle are, however, beyond the diagnostic capability of the measurement instruments. Therefore, the degree of match of the simulations have to be interpreted implicitly by comparing the diagnostically available parameters. The most important of these parameters are the global power balance and the separatrix density, which can be interpreted from the IRTV, the bolometry and the interferometry measurements.

The evolution of the pedestal n_e in EDGE2D/EIRENE simulations was observed to be comparable to the interferometry signal. The power crossing the separatrix was imposed as close to experimental values as achievable by imposing comparable ELM drop with durations of 1 and 0.2 ms. The 1 ms ELM demonstrated encouragingly similar dynamics compared to the experimental values of target power deposition, plasma radiation, pedestal density and plasma diamagnetic energy. The in/out asymmetry was inverted in the EDGE2D/EIRENE simulations presumably due to insufficient physics models in the simulation code. The ELM wetted areas were slightly underestimated, though, taken the crudeness of the approach and the cross-field transport model in fluid codes in general, the match can be seen as a satisfactory one. The electron contribution to the ELM target power

deposition was highly overestimated, presumably due to insufficient sheath model. Therefore, the 1 ms ELM provides probably as good a qualitative match to the SOL ELM evolution as is achievable with the present simulation approach. The qualitative evolution of the SOL parameters are reproduced on time scales longer than 1 ms. The detailed intra-ELM time-evolution of the plasma parameters may not be, however, reproduced. The 0.2 ms ELM leads generally to a factor of five too rapid dynamics compared to experimental values. Therefore, although the 0.2 ms ELM presumably imposes separatrix crossing power closer to experimental values, the total power exhaust dynamics in EDGE2D/EIRENE become too rapid if such SOL input powers are used in the ELM simulations.

The ELMs are anticipated to lead to a sequence of increased target temperature followed by increased target density, by imposing a cycle through the different SOL plasma regimes. The question whether EDGE2D/EIRENE is capable in simulating this cycle reliably depends essentially on the ability of EDGE2D/EIRENE to model transients between different SOL regimes. Apparently, a qualitative match to the experimental signals on time-scales larger than 1 ms can be obtained as has been demonstrated in this study as well as in [68]. Matching the detailed time-evolution in the time-scales shorter than 1 ms may, however, be beyond the computational capability of EDGE2D/EIRENE at least as long as substantial kinetic corrections are not employed.

4 Tungsten Transport Simulations

4.1 Description of the DIVIMP Simulations

Tungsten erosion and transport are simulated in this study by employing the Monte-Carlo test particle trace-ion code DIVIMP on the ELM background plasmas dynamically evolved with EDGE2D/EIRENE. A series of background plasmas is produced from each of the simulated ELMs in EDGE2D/EIRENE. The average time interval between consecutive ELMs in the simulated discharge was around 40 – 50 ms corresponding to the ELM frequency of 20 – 25 Hz. The interval between consecutive background plasmas in the produced set of series is 100 μs during $t - t_{\mathrm{ELM}} \in$ [-0.1 ms, 1.9 ms], 1 ms during $t - t_{\mathrm{ELM}} \in$ [1.9 ms, 10.9 ms] and 10 ms during $t - t_{\mathrm{ELM}} \in$ [10.9 ms, 40.9 ms]. DIVIMP is used on a steady-state fashion on the different background plasmas to calculated the erosion of tungsten and the fraction of eroded particles leaking to core. Tungsten core leakage is interpreted from the DIVIMP simulations by multiplying the tungsten erosion rate at the current time slice, $\Gamma_{\mathrm{W}}^{\mathrm{erosion}}(t)$, with an average core leakage fraction within a certain set of the following time slices. The duration of the averaging procedure is determined by the average time it takes an impurity particle to cross the LCFS in the DIVIMP simulation corresponding to the time-slice t, $\Delta t_{\mathrm{LCFS}}^{\mathrm{cross}}(t)$:

$$\Gamma_{\mathrm{W}}^{\mathrm{core}}(t) \approx \Gamma_{\mathrm{W}}^{\mathrm{erosion}}(t) \frac{\int_t^{\Delta t_{\mathrm{LCFS}}^{\mathrm{cross}}(t)} f_{\mathrm{leakage}}(\tau) d\tau}{\int_t^{\Delta t_{\mathrm{LCFS}}^{\mathrm{cross}}(t)} d\tau}. \tag{22}$$

The $\Delta t_{\mathrm{LCFS}}^{\mathrm{cross}}$ values obtained in this study are around 200 – 500 μs during the intra-ELM phase and approximately 500 – 1500 μs during the ELM recovery phase.

Tungsten confinement time is calculated according to equation (18) giving an order of magnitude estimate of 15 ms. Here $D_{\perp}^{\mathrm{SOL}} \sim 1$ m^2/s, $f_{\mathrm{ELM}} \sim 20$ Hz, $L_{\parallel}/c_{\mathrm{s,\,W}} \sim 1.7$ ms, $T_{\mathrm{e}}^{\mathrm{ped}} \sim 800$ eV, $T_{\mathrm{W}}^{\mathrm{ped}} \sim 800$ eV and $L_{\parallel} \sim 50$ m have been assumed. In the section 2.4, it was deduced that the equation (18) may not be perfectly valid for the JET ILW discharges. Conducting full core transport simulations are, however, well beyond the scope of this study. Therefore, this equation is used to give an approximative order of magnitude estimate, which is anticipated to be more reliable than just neglecting the effect of ELMs and using Bohm-like 1 s confinement time. Using these values with $n_{\mathrm{e}}^{\mathrm{core}} \approx 7 \cdot 10^{19}$ m^{-3} and $V_{\mathrm{core}} \approx 100$ m^{-3}, the core tungsten concentration estimates in this study are calculated, according to the

equation (15), by:

$$c_W \approx \frac{f_{ELM}\tau_W^{conf.}\int_{ELM\text{-}cycle}\Gamma_W^{core}(t)dt}{V_{core}n_e^{core}} = 4.3N_W^{ELM}\,[10^{-6}], \tag{23}$$

where the amount of tungsten leaking to the core plasma per ELM cycle, N_W^{ELM}, is given in units [10^{17} #]. Assuming a flat core temperature profile of about 1700 keV, the equation (1) gives an estimate for the tungsten radiative power:

$$P_Z^{rad} \approx 2.5 \cdot 10^5 c_W\,[\mathrm{MW}]. \tag{24}$$

The tungsten radiative power varies by a factor of 2 – 3 within the temperature range of 1000 – 2000 keV. This can be taken as the error estimate caused by the assumption of the flat core temperature. This is overwhelmed by the error bars caused by the factor of 10 – 100 uncertainties in the core confinement time. Essentially, the accuracy of the obtained estimates is, at best, order of magnitude, and the error bars are comparable to factors of at least 10.

Tungsten erosion due to background deuterium and 1% carbon 4+ contamination are taken into account. The carbon represents the presence of low-Z impurities in the plasma. The sputtering yield for deuterium impact is taken from [56] and for carbon impact from [84]. The tungsten self-sputtering is not included in the calculations but is investigated in a separate set of simulations. The prompt re-deposition of tungsten particles is taken into account. The transport of tungsten atoms is calculated with the neutral code EIRENE [9]. The atomic rates for tungsten are taken from the ADAS 97 database [85]. The transport of tungsten ions is calculated in the parallel-**B** direction according to the fluid force (equation (17)), and the cross-field transport is assumed to be diffusive with a diffusion coefficient of 1 m^2/s. To address the issue raised by Reiser [58] about the validity of the fluid force calculations, an additional set of simulations is conducted with the drift-kinetic parallel-**B** forces as suggested in [58].

4.2 Predictions for Tungsten Contamination

The elevated target temperatures during the intra-ELM period leads to significantly increased tungsten sputtering and initial velocity of the sputtered atoms, while the background deuterium friction is considerably lowered due to the lowered plasma collisionality (figure 24). Accordingly, the plasma contamination rate is significantly increased during the ELM temperature onset at the targets. The simulated ELMs in EDGE2D/EIRENE lead to a rapid increase of the target temperature followed by an

increase of the target density. The electron temperatures at the targets rise rapidly to a few 100 eV after the ELM onset and remain elevated during the first few 100 μs of the ELM event. The target densities drop by a factor of five during the first few 100 μs and rise then to values of a factor of five above the pre-ELM ones roughly 1 ms after the ELM onset . The target density remains elevated at the inner target roughly 5 ms after the ELM onset and at the outer target as long as 30 ms after the ELM onset. The elevated target density leads to high-recycling divertor plasma conditions, which lower the target plasma temperature rapidly to a few 10 eV. Once the target density rises, the target temperature drops while the plasma collisionality increases. Therefore, the divertor sputtering and the initial velocity of the sputtered atoms are lowered while the background friction is increased, thus considerably suppressing the core contamination rate. Therefore, the results for the 1 ms medium $D_\perp$ multiplier ELM simulation suggest that the core tungsten contamination of the high pedestal pressure ELMy H-mode plasmas is highly dominated by the relatively short intra-ELM period (figure 24). As the dominant core out flux of impurities in the H-mode plasmas is presumably imposed by the ELM caused core purging, the tungsten contamination of the ELMy H-mode plasmas becomes a balance process determined dominantly by the characteristics of the ELMs. They impose not only the dominant core purging process, but also the principal core contamination source. The results obtained here are consistent with the experimental observations on ASDEX upgrade tokamak for ELMy H-mode plasmas documented in [86].

These simulations provide an order of magnitude of 10^{17} tungsten particles entering the core plasma during an ELM cycle leading to estimates of $c_W \approx 5 \cdot 10^{-6}$ and $P_Z^{rad} \approx 1.5$ MW using the equations (24) and (23). These should, however, be interpreted only as approximative order of magnitude estimates due to the uncertainty of the core confinement time of a factor of at least 10 – 100. Furthermore, the evolution of the main chamber material configuration is not followed in this study, and the contribution to the tungsten contamination caused by the tungsten deposited at the main chamber walls remains uncertain. The main chamber deposition increases the effective upstream confinement time of tungsten, which would probably increase the tungsten core concentration. This is, however, an issue, which needs to be investigated in detail in subsequent studies. Nevertheless, it would seem plausible that the core contamination caused by the main chamber deposited tungsten would also be dominated by ELMs, due to the significant intra-ELM main chamber power depositions. On the other hand, charge exchange neutrals and ions accelerated by ICRH may cause considerable main chamber erosion during the inter-ELM phase. Accordingly, without further studies the effect of the main chamber deposition to

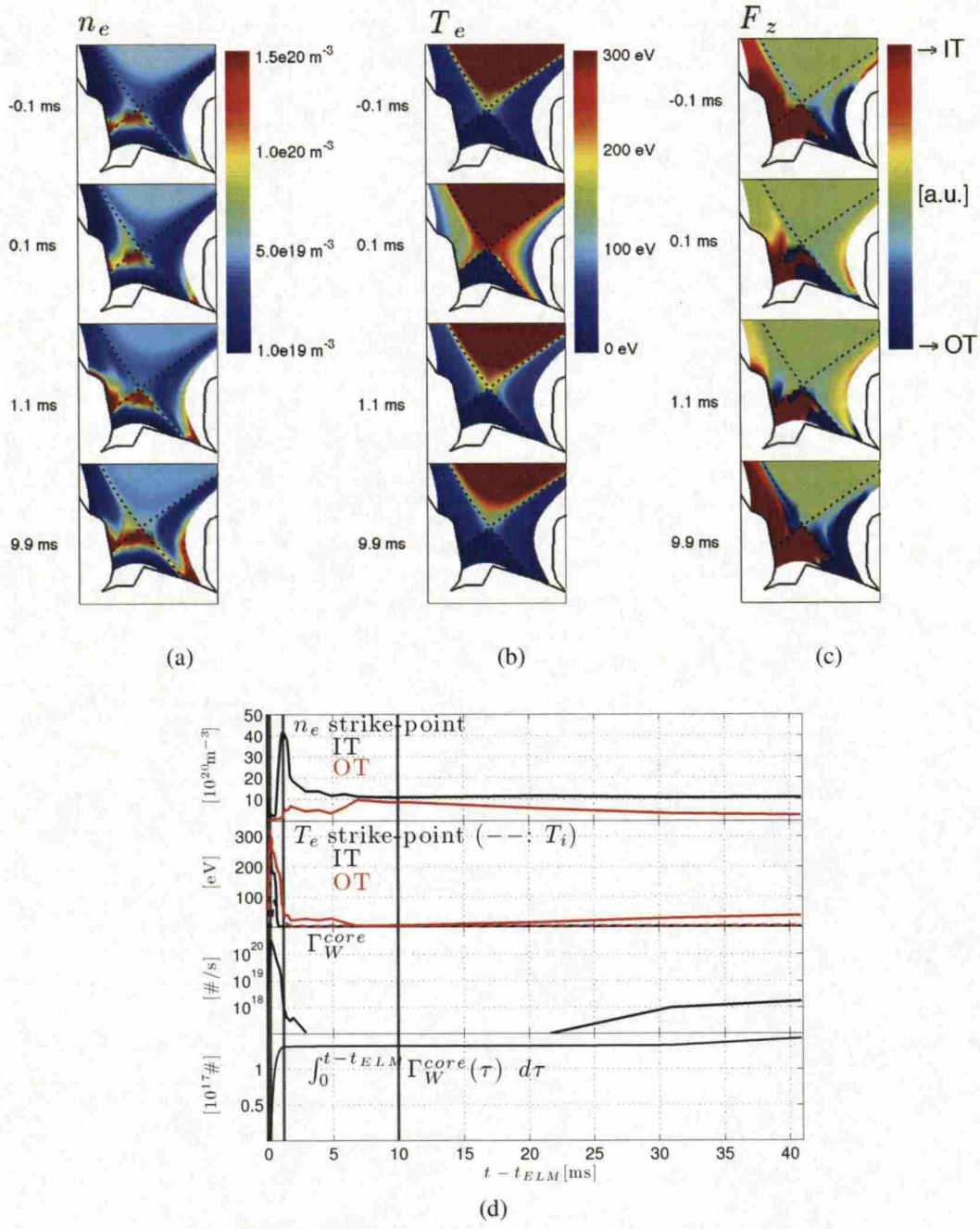

Figure 24: Contour plots of divertor electron density (a), temperature (b) and average parallel-**B** fluid force on impurity particles with charge states 1 – 10 (c) for the base case medium $D_\perp$ multiplier 1 ms ELM. In the figure c), the blue colour stands for force towards the outer target (OT) and the red colour for force towards the inner target (IT). d) Time traces of the electron density and temperature at the strike-points as well as the core W leakage rate and the integrated core W contamination over the ELM cycle. The dark grey lines represent the time-slices of the contour plots.

the core contamination cannot be determined.

Similar results to the ones found here were obtained in [87], where the ELMs

were found to lead to strong increase of target sputtering and divertor leakage in simulations utilizing DIVIMP on background plasmas dynamically evolved with an integrated code-suite JINTRAC [80] for a low triangularity and low collisionality ITER-like wall reference JET discharge 73569 [81]. The plasmas in [81] were simulated with W/Be wall configuration including various levels of Neon seeding.

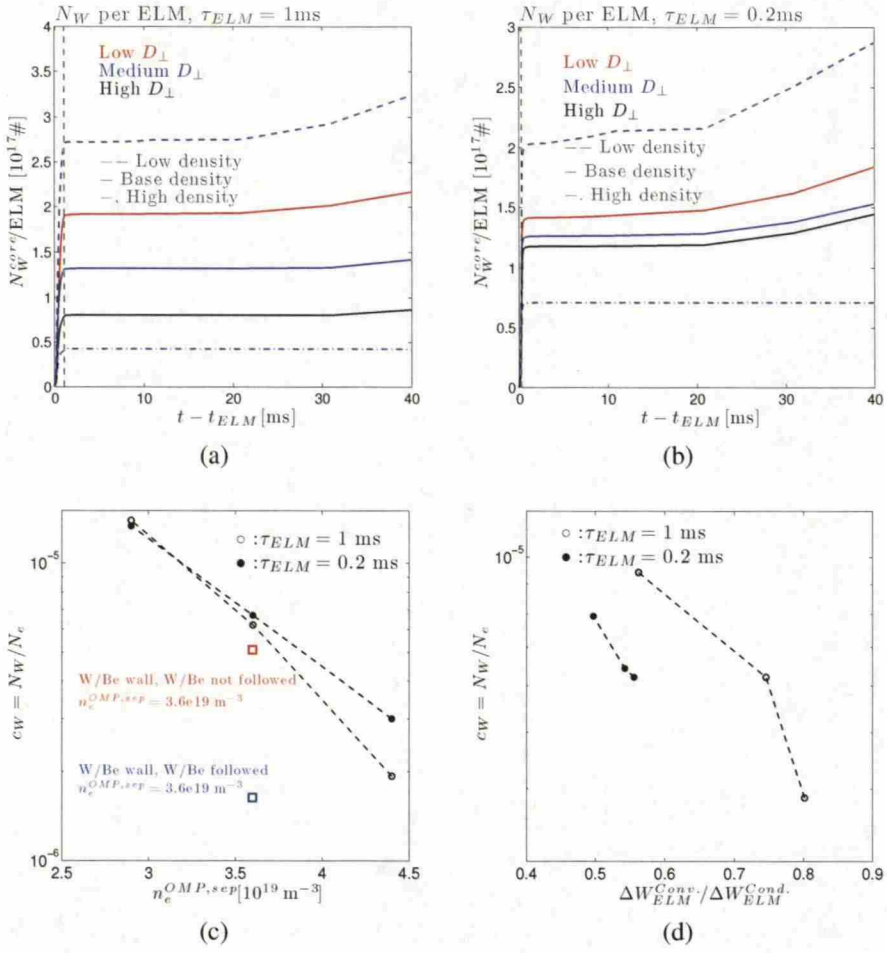

Figure 25: The amount of tungsten entering the core per an ELM cycle: a) 1 ms; b) 0.2 ms. The predicted tungsten concentration: as a function of the plasma density (c); as a function of the ratio of the convective ELM losses to the conductive ones (d). The W/Be wall cases are obtained by changing the main chamber wall in the simulations from CFC to W/BE and setting up a density feedback to maintain the separatrix electron density. The red case is simulated as pure-D plasma, and the blue case by following the sputtering and transport of tungsten and beryllium in the plasma.

The obtained order of magnitude of 10^{17} particles entering the core per an ELM cycle scales weakly in plasma density, ELM magnitude and ELM duration (figure 25). Taking the significant difference in the magnitudes of the target power depositions between the 1 and 0.2 ms ELM cases (figure 18), this results seems rather surprising. It seems that the higher temporal power deposition in the 0.2 ms ELM case is compensated by the shorter duration such that the total tungsten con-

tamination is not much different compared to the 1 ms case. For the low and high density plasmas, medium $D_\perp$ multiplier ELMs with the two durations are considered.

The core contamination decreases with increasing plasma density and with increasing ratio of the convective ELM losses to the conductive ones (figure 25c and d). Within the spanned parameter range, the reduction is not, however, orders of magnitude, but rather a factor of $5-7$ reduction is obtained by increasing the $n_e^{\text{OMP sep}}$ from $2.9 \cdot 10^{19}$ m^{-3} to $4.4 \cdot 10^{19}$ m^{-3}. Within the spanned range in the convective-conductive ELM-ratio the reduction is only within a factor of 2 – 3. It should be noted, however, that the tungsten core contamination in the study actually decreases as a function of increasing ELM magnitude, as the variations in the ELM loss ratios are obtained by scaling the $D_\perp$ multiplier (figure 25d, table 3). Therefore, it is concluded that the increased convective-conductive ELM-ratio boosts the divertor collisionality during the intra-ELM phase, thus reducing the magnitude of the ELM related impurity leakage. Accordingly, the obtained scalings suggest that the plasma tungsten contamination decreases with increasing plasma collisionality, mainly due to increased divertor plasma friction and increased convective-conductive ELM-ratio, which leads to enhanced intra-ELM divertor collisionality. The intra-ELM divertor collisionality appears to be the dominant factor determining the core contamination.

The background plasmas in EDGE2D/EIRENE in this study were simulated with a CFC wall configuration. Those background plasmas were used for predicting tungsten erosion and transport in JET ILW discharges. The neutral recycling properties of the CFC and the W/Be PFCs are not, however, identical, which may, consequently, lead to differences in the plasma solutions and, eventually, in the predictions obtained for the tungsten erosion and transport. To address this issue, two additional EDGE2D/EIRENE background plasma series were produced. These plasmas were simulated by taking the 1 ms medium $D_\perp$ multiplier ELM case and changing the wall configuration to W/Be and setting a density feedback to obtain the same OMP separatrix electron density as with the carbon wall. The first one of these cases was simulated as pure deuterium plasma, and the other by taking into account the tungsten and beryllium sputtering and transport in the plasma. The predicted tungsten concentrations in the plasma are not changed significantly (figure 25c). The pure deuterium case predicts a reduction of the tungsten contamination by a factor of two compared to the CFC wall case. It should be noted that the DIVIMP simulations are still conducted with 1% carbon contamination. Only the background plasma is affected by the pure deuterium assumption. The

inclusion of tungsten and beryllium impurities in the EDGE2D/EIRENE simulation leads to a factor of five reduction in the tungsten contamination predicted by DIVIMP compared to the corresponding CFC wall case. The effect of tungsten in the EDGE2D/EIRENE simulations is to drop the outer mid-plane separatrix temperatures: T_e: 118 eV $\rightarrow$ 113 eV and T_i: 219 eV $\rightarrow$ 182 eV. The power crossing the separatrix is reduced by 200 kW after including tungsten in the simulation. Therefore, tungsten impurity lowers the target temperatures, leading to lower tungsten erosion and to higher target collisionality, which reduces the core leakage. The simulated tungsten contamination in EDGE2D/EIRENE is, however, obtained by the steady-state pre-ELM tungsten erosion and transport, and does not, therefore, represent a realistic tungsten contamination in ELMy H-mode plasmas. Instead, the obtained values give a first order sensitivity estimate for the plasma properties in the case of tungsten contamination, providing insight to the effect. The detailed effect of the tungsten contamination to the background plasma properties in ELMy H-mode plasmas needs to be further investigated in subsequent studies.

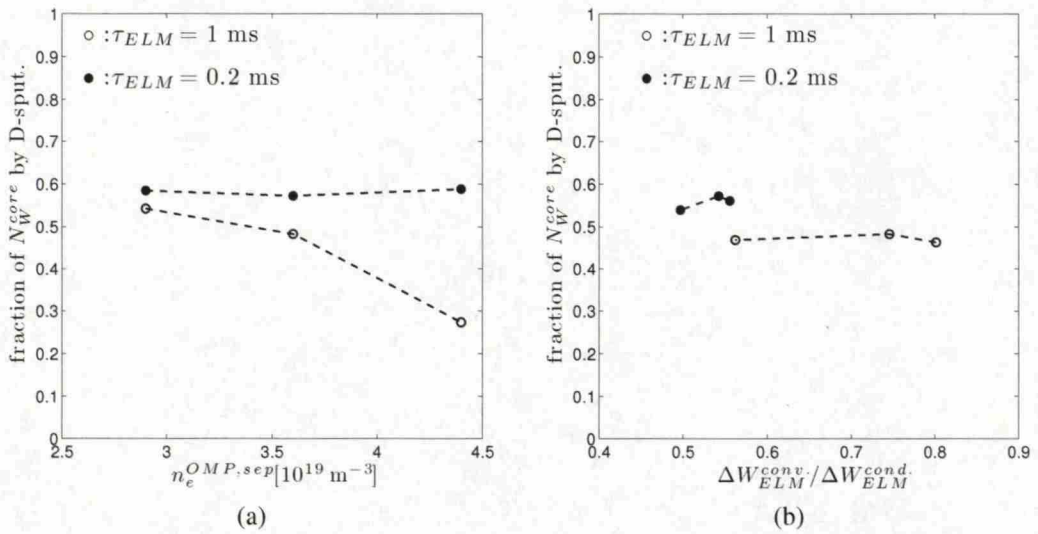

Figure 26: The fraction of the core tungsten contamination caused by deuterium sputtering: as a function of the plasma density (a); as a function of the ratio of the convective ELM losses to the conductive ones (b).

Approximately half of the tungsten contamination is caused by sputtering due to deuterium impact, within the obtained density and ELM magnitude scans (figure 26). Tungsten self-sputtering is neglected here. As most of the tungsten contamination occurs during the intra-ELM period, the sputtering due to deuterium contributes significantly to the core contamination. Accordingly, the achievement of pure deuterium plasma conditions at the target would reduce the core contamination only by a factor of two. On the other hand, according to the results, the core contamination

would not be enhanced significantly by the increased sputtering entailed by SOL plasma seeding. Actually, the SOL plasma seeding would presumably reduce the core contamination, as the sputtering and divertor leakage decrease strongly with decreasing divertor plasma temperatures. In the case of the 1 ms ELMs the fraction of tungsten contamination caused by deuterium sputtering decreases with increasing plasma density reaching the level of about 30% in the highest simulated density. This is associated with the lower target temperatures in the higher density plasmas. The 0.2 ms ELMs do not show similar scaling due the extremely high temporal target power depositions in those simulations, therefore causing high tungsten deuterium sputtering yields regardless of the plasma density.

The self-sputtering of tungsten was not included in the main simulations in this study. An additional simulation for the base case 1 ms medium $D_\perp$ multiplier ELM demonstrates that during the intra-ELM period the tungsten self-sputtering can lead to a short duration run away process, thus enhancing the intra-ELM tungsten source and, accordingly, the core tungsten contamination considerably (figure 27a). During the inter-ELM phase the tungsten self-sputtering increases the tungsten source roughly by 10%. The self-sputtering enhancement factor is determined as the percentage that the self-sputtering increases the sputtering magnitude compared to simulation without self-sputtering.

The actual realistic self-sputtering enhancement to the intra-ELM sputtering remains, however, uncertain. The energy of the self-sputtering particles impacting the solid surface is largely determined by the acceleration through the sheath electric field. The duration and the magnitude of the elevated target temperature during the intra-ELM phase is poorly known, thus leaving the actual intra-ELM accelerator potential uncertain. The figure 27b illustrates the charge state distribution of tungsten in front of the outer strike-point during the ELM onset at the target. Comparing to the figure 27c, it is observed that over 90% of the particles ($Z \geq 2$) in front of the outer strike-point in the model gain sufficient energy through the sheath potential to cause sputtering yield over unity (figure 27d). The sheath acceleration is calculated here as it has been calculated in the simulations: $V_{sf} \sim -3T_e/e$. In reality, the intra-ELM sheath potential is, however, anticipated to be much stronger than this due to the supra-thermal electron burst during the ELM onset charging the wall negatively. Therefore, the self-sputtering yield of unity could be achieved with lower target temperatures than has been assumed in the model. On the other hand, the duration of the elevated sheath potential during the intra-ELM phase is not known, and it might be short enough to prevent significant self-sputtering run-away cascades from occurring. Therefore, the effect of the self-sputtering in practice may

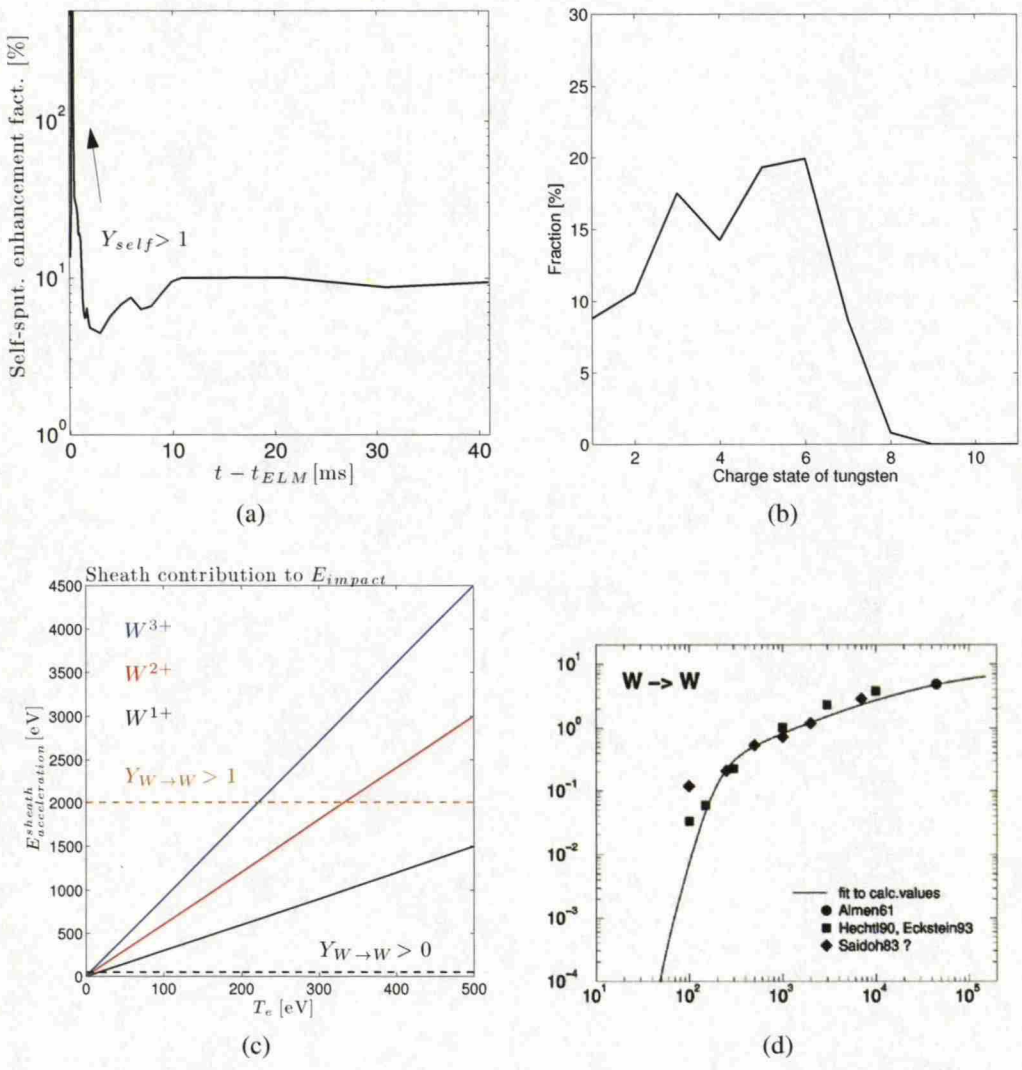

Figure 27: a) Self-sputtering enhancement factor calculated for the 1 ms medium $D_\perp$ multiplier base case ELM. b) Charge state distribution of tungsten in front of the outer strike-point during the ELM onset (target $T_e \sim 300$ eV) in the DIVIMP self-sputtering simulation. c) Sheath acceleration contribution to impact energy as a function of the target electron temperature for tungsten with charge states 1+ (black), 2+ (red), and 3+ (blue). $V_{sf} \sim -3T_e/e$ has been assumed. During the intra-ELM phase, the sheath potential is, in reality, much stronger due to the supra-thermal electron burst. It is observed that for target electron temperature of 200 eV, the tungsten 3+ gains sufficient momentum to cause sputtering yield of unity. For tungsten 2+, the corresponding temperature is 300 eV. d) Tungsten self-sputtering yield as a function of normal incidence impact energy as given in [56].

as well be to enhance the sputtering magnitude slightly, but not necessarily lead to catastrophic tungsten erosion cascades. Within this study, this cannot be further addressed, and this issue must be further investigated in subsequent studies.

The DIVIMP simulations in this study are conducted by using the parallel-**B** fluid forces [88]. It has been, however, demonstrated in [58] that this approach may become invalid in the case of significant velocity difference between the test

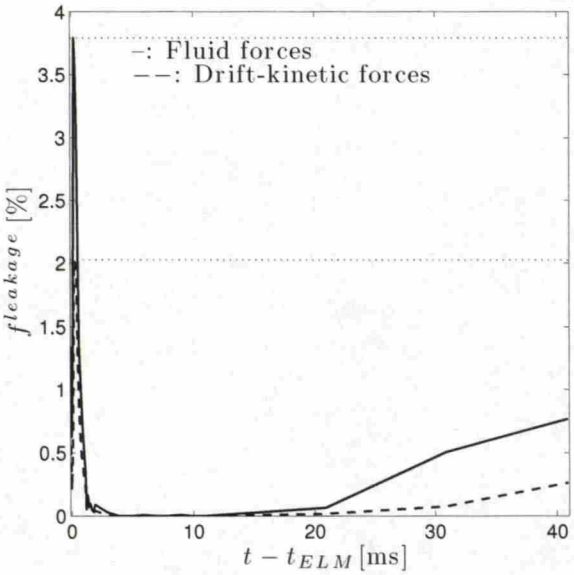

Figure 28: The leakage percentages predicted by the fluid forces as well as by the drift-kinetic forces for the 1 ms medium $D_\perp$ multiplier base case ELM. The drift-kinetic forces lead to approximately a factor of two lower leakage in intra-ELM low collisionality plasmas. In the pre-ELM moderate collisionality plasmas, the fluid forces predict a factor of 4 – 6 lower leakage. Therefore, the fluid forces may overestimate slightly by a factor of < 5 the divertor leakage, but the obtained ELM dynamics are not changed, i.e. strong increase of divertor leakage due to ELMs.

particles and the background deuterium flow. To address this issue, an additional simulation for 1 ms medium $D_\perp$ multiplier ELM base case was conducted employing the drift-kinetic parallel-**B** forces as has been suggested in [58]. It is observed that the core leakage fraction is reduced roughly by a factor of two during the ELM onset compared to the fluid force simulations (figure 27). During the ELM recovery phase, the divertor plasma collisionality is high enough to ensure a small velocity difference between the background particles and impurities, therefore leading to similar results between the two approaches. As the background plasma evolves towards the pre-ELM phase, the divertor collisionality drops and, consequently, > 20 ms after the ELM onset, the fluid forces begin to predict a factor of 4 – 6 higher leakage. The tungsten sputtering here is, however, dominated by the intra-ELM period, and thus the factor of five deviations during the pre-ELM phase do not change the final solution, which is mainly determined by the intra-ELM period. Accordingly, the order of magnitude obtained by the fluid force approach is not considerably amended in the drift-kinetic approach.

5 Conclusion

Tungsten erosion and transport have been simulated for one of the JET ITER-like wall reference plasmas of high triangularity by using the quasi-kinetic Monte Carlo trace-ion code DIVIMP. The simulations are based on background plasmas simulated and dynamically evolved with the 2-D multi-fluid code EDGE2D/EIRENE. The ELMy H-mode background plasmas are simulated by obtaining first steady-state EDGE2D/EIRENE solutions benchmarked to the pre-ELM measurements of n_e and T_e at the outer mid-plane by high resolution Thomson scattering and to the target T_e, j_{sat} and q values measured by the Langmuir probes and the infra-red camera. ELMs are simulated based on the obtained pre-ELM cases by imposing short duration enhancements for the cross-field diffusion coefficients around the outer mid-plane. The ELM model is adjusted to provide a match within a factor of two to the total ELM pedestal energy losses and to the ratio of the convective ELM losses to the conductive ones. The obtained ELM solutions are used as time-evolving series of background plasmas in the DIVIMP calculations of tungsten erosion and core leakage. Tungsten erosion due to background deuterium and small percentages of light impurities, represented by 1% carbon 4+ contamination, has been taken into account.

The simulated ELMs in EDGE2D/EIRENE lead to target temperatures excess of 200 eV. The target temperatures remain elevated during the first few 100 μs of the ELM event. Roughly 1 millisecond after the ELM onset, the target densities begin to rise. These density-temperature dynamics lead to a considerable increase of the target sputtering and the divertor leakage of tungsten during the sheath-limited high target temperature phase of the simulated ELM. Once the target density rises, the target conditions evolve towards high recycling ones lowering the target temperature rapidly, thus reducing the target sputtering and divertor leakage considerably. Consequently, in the simulations the ELMs produce the dominant contribution to the core tungsten contamination. Therefore, the core tungsten contamination of ELMy H-mode plasmas becomes a balance process between the ELM core purging, and the ELM caused core contamination, thus being ultimately determined by the ELM characteristics.

Tungsten concentrations of the order of $10^{-6} - 10^{-5}$ were obtained for a range of plasma densities and ELM characteristics. The tungsten contamination was observed to decrease with increasing plasma collisionality. These estimates were obtained omitting self-sputtering. In an additional simulation, it was observed that the self-sputtering leads to a considerable increase of the impurity source during the

intra-ELM phase. Therefore, the self-sputtering is anticipated to increase the contamination values above to the obtained estimates. The actual amount of erosion caused by self-sputtering remains, however, uncertain as long as detailed time-evolution of the sheath potential during the intra-ELM phase is not considered. Therefore, the questions, how much the intra-ELM sputtering is enhanced by self-sputtering, whether it is a factor of 5 or 500, cannot be addressed within this study. The fraction of the tungsten contamination caused by sputtering due to deuterium impact, omitting self-sputtering, was calculated to be roughly 50%, decreasing slightly with increasing plasma density, reaching roughly 30% in the highest density case.

The detailed ELM power balance was not matched to the experimental estimations. The amount of ELM energy deposited at the target plates was roughly reproduced, but the calculated in/out asymmetry was inverted compared to the experimental observations. EDGE2D/EIRENE calculates two times as much ELM power deposition at the outer target as at the inner target, whereas the IRTV measurement in JET normal field discharges show typically opposite behaviour. Moreover, the ELM parallel-**B** power transport is overestimated in EDGE2D/EIRENE causing ELM power transit time-scales of 0 – 100 μs compared to the experimental observations of 100 – 300 μs. The ELM energy transport in EDGE2D/EIRENE is highly dominated by the fast electron conduction channel, whereas, according to the experimental observations, the ELM energy transport is interpreted to be dominated by ion sound-speed convection. This issue relates to the fluid approach of EDGE2D/EIRENE, which is insufficient for reproducing the evolution of kinetic effects, such as ELMs. The kinetic corrections used in the simulations here are insufficient to reproduce the electron-ion ratio in the power transport, which leads to overestimated power transport in the time scales comparable to the electron transit time: ~ 3 μs. The predictive capability of the model in this study is, thus, strongly limited by the inability of EDGE2D/EIRENE to model the short time-scales of the ELM event reliably. The model, nevertheless, provides a qualitative description of the divertor plasma evolution in ELMy H-mode plasmas. The details of divertor plasma dynamics appear to be, however, biased by the too fast power transport via the electron conduction channel leading to very high intra-ELM target electron temperatures. Accordingly, the target intra-ELM electron temperatures are prone to be overestimated in the EDGE2D/EIRENE simulations. The high electron target temperatures lead generally to high core contaminations; therefore, the obtained tungsten core contamination rates can be overestimated. Consequently, taken the uncertainty imposed by the self-sputtering process, the error-bars in the obtained tungsten

contamination values remain significant. The magnitudes of these error bars cannot be addressed within this study, but a detailed comparison to experimental JET ILW discharges as well as to kinetic PIC simulations is required to gain further insight to this issue. The simulated cycle of significantly increased core contamination during the intra-ELM phase, followed by considerably suppressed contamination during the ELM recovery phase is, nevertheless, plausible to be qualitatively feasible as long as ELMs are anticipated to lead to increased target temperatures of the order of 100 – 300 eV followed by increased target densities within the ion sound-speed time-scales. Therefore, qualitative insight to the tungsten erosion and transport dynamics in JET ELMy H-mode plasmas is obtained in this study, and this insight will be enhanced in following studies.

Discussion

The ELM evolution was qualitatively reproduced in the EDGE2D/EIRENE simulations in this study. To further enhance the predictive capability of the global ELM SOL simulations, both significant kinetic corrections, and enhanced experimental diagnostic capability of the ELM events are required. To obtain full time-evolving ELM fluid modelling including the core, the integrated code suite JINTRAC [80] should be used in the subsequent studies, instead of EDGE2D/EIRENE as stand alone. JINTRAC as such would, however, suffer from similar drawbacks as EDGE2D/EIRENE. The fluid simulations of kinetic phenomena, such as ELMs, require significant kinetic corrections to match the dynamics, which are largely related to the electron-ion and to the conductive-convective balances. Further uncertainty to the simulations is related to the electron-ion balance of the actual pedestal ELM drop. Detailed experimental data of this balance is not available. Therefore, probably the best approach for simulating ELMy plasmas globally in a fusion reactor with the fluid codes is to impose a temporal energy source into the SOL, and benchmark that energy source to the estimated ELM magnitudes and to the convective and convective ELM losses. To reproduce the electron-ion balance in the ELM losses, a sensitivity scan is required due to the missing experimental information. Once the upstream electron-ion ratio in the model is reproduced, the kinetic corrections in the SOL transport can be employed to obtain as close to reality as possible temporal evolution of the SOL density and temperature.

The most important kinetic corrections are presumably the sheath-heat transmission coefficients, which need to be evolved over the ELM deposition at the target to take into account the kinetic evolution of the sheath potential. The second order correction would be given by time-evolving heat-flux limiters to limit the conductive heat-flux in the beginning and in the end of the ELM event, i.e. during the periods of parallel-**B** temperature gradients in the SOL. These corrections should cut down the electron power transport contribution, which would already give rather good time scale agreements in the model. Finally, the third order correction could be introduced by using the parallel-**B** ion viscosity limiter, which, according to PIC and fluid model comparisons done in [89], would presumably slow down the ion power transport suitably to further enhance the match of the dynamics between the experimental and ion power transport signals.

To benchmark the time scales of the parallel-**B** power transport, one should compare the electron power transport to the experimental soft X-ray signal and the ion transport to the IRTV signal. Further, one would need to match the target neutral re-

cycling rate interpreted from the D_α signal. This was not addressed in this study, but will be included in following studies. To benchmark the divertor radiation balance during the intra-ELM phase, a high time resolution bolometer diagnostic would be required. The 200 Hz system available in this study, was too slow to enable a detailed analysis of the radiation dynamics in the divertor.

The inverted in/out asymmetry in EDGE2D/EIRENE could presumably be shifted towards the experimental observations by imposing the ELMs at the inner side of the poloidal cross-section. This would, however, be a completely *ad hoc* approach trying to match the target conditions by compromising the upstream ones. This approach would contradict the ELM losses dominantly occurring the LFS side consistent with the ballooning characteristics of ELMs. Accordingly, justifying this approach would be challenging. Matching the detailed global ELM time-evolution may, however, be beyond the simulation capability of the 2-D fluid codes due to insufficient physics models. Another possible approach, would be to impose an artificial flow towards the inner target on the particles crossing the OMP separatrix in the ELM simulations.

To model the erosion and transport of tungsten, the most important experimental quantities to match are the target temperatures and density. Obtaining experimental estimates for these over an ELM cycle would be very beneficial for the predictive simulations of target sputtering and impurity transport. Actually, experimental data of those parameters would enable an onion-skin-model (OSM) [23] analysis of tungsten erosion and transport with exact measured target parameters.

To gain further insight to tungsten erosion and transport, kinetic PIC ELM simulation of self-consistent tungsten erosion and transport are of strong interest. These kinetic studies are, however, computationally heavy and cannot generally include a realistic machine geometry with a realistic 2-D neutral profile in the divertor. Therefore, the best achievable result will be obtained by cross-comparing the results obtained with the different simulation approaches.

The results obtained here will in near future be compared to experimental measurements of tungsten contamination in the ILW discharges. According to this study, the tungsten contamination is anticipated to decrease with increasing plasma collisionality and with impurity seeding. Therefore, decreasing core tungsten signals should be observed with increasing fuelling and seeding. The experimental measurements of the time-evolution of tungsten erosion and core contamination can be further compared to the obtained simulated dynamics.

Acronyms

The acronyms used in this study.

CFC	Carbon-fibre composite
ECE	Electron cyclotron emission
EFIT	Magnetic equilibrium reconstruction
ELM	Edge localized mode
ETB	Edge transport barrier
EVDF	Electron velocity distribution function
H-mode	High confinement mode
HFS	High field side
HRTS	High resolution Thomson scattering
ICRH	Ion cyclotron resonance heating
ILW	ITER-like wall
IRTV	Infra-red camera
IT	Inner target
ITER	International Thermonuclear Experimental Reactor
JET	Joint European Torus
JPN	Jet pulse number
L-mode	Low confinement mode
LCFS	Last closed flux surface
LFS	Low field side
LP	Langmuir probe
MHD	Magnetohydrodynamic
NBI	Neutral beam injection
OMP	Outer mid-plane
OSM	Onion-skin-model
OT	Outer target
PFC	Plasma-facing component
PFR	Private flux region
PIC	Particle-in-cell
PSI	Plasma-surface interaction
SE	Sheath edge
SOL	Scrape-off layer

Symbols

The main symbols used in this study. The symbols which are defined each time they appear in the text are not listed here.

n_σ	Density of the species σ [m^{-3}]
T_σ	Temperature of the species σ [eV]
p_σ	Pressure of the species σ [Pa]
W, E	Energy [J]
P	Power [W]
q	Power flux [W/m^2]
Γ	Particle flux [$m^{-2}s^{-1}$]
t	Time [s]
v	Plasma flow velocity [m/s]
c_s	Plasma sound speed [m/s]
c_σ	Sound speed of the species σ [m/s]
$L_\parallel$	Parallel SOL connection length [m]
V_{sf}	Floating potential [V]
τ_{ELM}	ELM duration [s]
t_{ELM}	ELM onset [s]
v_{pinch}	Cross-field convection [m/s]
$D_\perp$	Cross-field diffusion [m^2/s]
$\chi_\perp$	Cross-field conduction [m^2/s]
f_{ELM}	ELM frequency [Hz]
j_{sat}	Ion saturation current density [A/m^2]
γ_σ	Sheath-heat transmission coefficient of the species σ
$\mathbf{E}$	Electric field [V/m]
$\mathbf{B}$	Magnetic field [T]
Z	Charge-state
Q	Fusion gain factor
D_α	Hydrogenic α Balmer line
ν^*_σ	Collisionality of the species σ
V	Volume [m^3]
R	Major radius of the plasma [m]
a	Minor radius of the plasma [m]
b	Half-height of the plasma [m]
B_Φ	Magnitude of the toroidal magnetic field [T]
B_θ	Magnitude of the poloidal magnetic field [T]
B_{total}	Total magnitude of the magnetic field [T]
I_Φ	Plasma current [A]
δ	Plasma triangularity
n_{GW}	The Greenwald density limit [m^{-3}]
q_{95}	The safety-factor at the 95% flux surface

References

[1] Shafiee, S. & Topal, E. *Energy Policy* **37**, 181 – 189, (2009)

[2] Meinshausen, M. *et al. Nature* **458**, 1158 – 1162, (2009)

[3] Matthews, G. F. *et al. Phys. Scr.* **T145**, 014001, (2011)

[4] Hawryluk, R. J. *et al. Nucl. Fusion* **49**, 065012, (2007)

[5] Pitts, R. A. *et al. Phys. Scr.* **T138**, 014001, (2009)

[6] Pütterich, T. *et al. Nucl. Fusion* **50**, 025012, (2010)

[7] Stangeby, P. C. & Elder, J. D. *Nucl. Fusion* **35**, 1391, (1995)

[8] Simonini, R. *et al. Contrib. Plasma Phys.* **34**, 368, (1994)

[9] Reiter, D. *Jour. Nucl. Mater.* **196 – 198**, 241, (1992)

[10] Wiesen, S. *EDGE2D/EIRENE code interface report*, JET ITC-Report, http://www.eirene.de/e2deir_report_30jun06.pdf, (2006)

[11] Einstein, A. *Annalen der Physik* **13**, 639 – 641, (1905)

[12] Wesson, J. *Tokamaks*, 3rd edition, Oxford University Press 2004, ISBN 0-19- 8509227

[13] Freidberg, J. P. *Plasma Physics and Fusion Energy*, Cambridge University Press 2007, ISBN-10 0-521-85107-6

[14] Keilhacker, M. *et al. Nuclear Fusion* **39**, 2, (1999)

[15] ITER physics basis, *Nuclear Fusion* **39**, 12 , 2137 – 2174, (1999)

[16] Pfalzner, S. *An Introduction to Inertial Confinement Fusion*, CRC press Inc. 2006, ISBN 0-7503-0701-3

[17] Mukhovatov, V. *et al. Plasma Phys. Control. Fusion* **45**, A235 – A252, (2003)

[18] EFDA-JET website, http://www.efda.org/2011/09/tokamak-principle-2/, 9.2.2012

[19] Freidberg, J. P. *Ideal Magnetohydrodynamics*, Springer 1987, ISBN 0-3064-2512-2

[20] Greenwald, M. *et al. Nucl. Fusion* **28**, 2199, (1988)

[21] Troyon, F. *et al. Plasma Phys. Control. Fusion* **26**, 209, (1984)

[22] EFDA-JET website, http://www.efda.org/fusion/focus-on/limiters-and-divertors/, 9.1.2012

[23] Stangeby, P. C. *The Plasma Boundary of Magnetic Fusion Devices*, IoP Publishing Ltd 2000, ISBN 0-7503-0559-2

[24] Hutchinson, I. H. *Principles of Plasma Diagnostics*, 2nd edition, Cambridge University Press 2002, ISBN 0-521-80389-6

[25] Gauster, W. B. *Nucl. Fusion* **30**, 1897, (1990)

[26] Roth, J. *et al. Plasma Phys. Control. Fusion* **50**, 103001, (2008)

[27] Paméla, J. *et al. Jour. Nucl. Mater.* **363 – 365**, 1 – 11, (2007)

[28] Federici, G. *et al. Jour. Nucl. Mater.* **313 – 316**, 11 – 22, (2003)

[29] Matthews, G. F. *et al. Phys. Scr.* **T128**, 137 – 143, (2007)

[30] Wagner, F. *et al. Phys. Rev. Lett.* **49**,1408 – 1412, (1982)

[31] Martin, Y. R. *et al. Jour. Phys.: Conf. Series* **123**, 012033, (2008)

[32] Wagner, F. *et al. Proc. 13th Int. Conf. Washington Vienna: IAEA* vol **1**, 277, (1990)

[33] Conway, G. D. *Plasma Phys. Control. Fusion* **50**, 124026, (2008)

[34] Kamiya, K. *et al. Plasma Phys. Control. Fusion* **49**, S43 – S62, (2007)

[35] Zohm, H. *Plasma Phys. Control. Fusion* **38**, 105 – 128, (1996)

[36] Suttrop, W. *Plasma Phys. Control. Fusion* **42**, A1 – A14, (2000)

[37] Loarte, A. *et al. Proc. 22nd IAEA Fusion Energy Conference*, 13 – 18 October 2008, Geneva, Switzerland, paper IT/P6-13

[38] Pitts, R. A. *et al. Journ. Nucl. Mater.* **390 – 391**, 755 – 9, (2009)

[39] Oyama, N. *et al. Nucl. Fusion* **43**, 1250 – 1257, (2003)

[40] Petrie, T. W. *et al. Nucl. Fusion* **43**, 910 – 913, (2003)

[41] Nunes, I. *et al. Nucl. Fusion* **44**, 883, (2004)

[42] Fundamenski, W. *et al. Jour. Nucl. Mater.* **363 – 365**, 319 – 324, (2007)

[43] Beurskens, M. N. A. *et al. Nucl. Fusion* **49**, 125006, (2009)

[44] Fundamenski, W. *et al.* Proc. 22nd Int. Conf. on Fusion Energy 2008 (Geneva, Switzerland,2008 **EX/4-3ra**, http://www-pub.iaea.org/MTCD/Meetings/FEC2008/ex_4-3ra.pdf, (2008)

[45] Loarte, A. *et al.* 2000 *Fusion Energy 2000*, ITERP/11(R): *Proc. 18th IAEA Fusion Energy Conf. (Sorrento, Italy, 2000)* (Vienna: IAEA)

[46] Spitzer, L. *The physic of Fully Ionized Gases*, 2nd edition, John Wiley & Sons Inc. 1962, ISBN 0-4708-1723-2

[47] Harrison, E. R. & Thompson, W. B. *Proc. Phys. Soc.* **74**, 145, (1959)

[48] Allen, J. E. *J. Phys. D: Appl. Phys.* **9**, 2331, (1976)

[49] Fundamenski, W. *et al. Plasma Phys. Control. Fusion* **47**, R163 – R208, (2005)

[50] Chodura, R. *Physics of Plasma-Wall Interactions in Controlled Fusion* ed D E Post and R Behrisch (New York: Plenum Press), 99, (1986)

[51] Chapman, S. & Cowling, T. G. *Mathematical Theory of Non-Uniform Gases*, Cambridge University Press, ISBN 978-0521408448

[52] Braginskii, S. I. *Reviews of Plasma Physics* vol I, ed Leontovich, M. A., p. 205, (1965)

[53] Schneider, R. *et al. Cont. to Plasma Phys.* **40**, 328, (2006)

[54] Fitzpatrick, R. *Plasma Physics, http://farside.ph.utexas.edu/teaching/plasma/*, 7.3.2012

[55] Spitzer, L. & Härm, R. *Physical Review* **89**, 977 – 981, (1952)

[56] Eckstein, W. *Sputtering by Particle Bombardment*, Springer-Verlag Berlin Heidelberg 2007, ISBN: 987-3-540-44500-5

[57] Eckstein, W., Bohdansky, J. & Roth, J. *Suppl. Nucl. Fusion* **1**, 51, (1991)

[58] Reiser, D., Reiter, D. & Tokar, M. Z. *Nucl. Fusion* **38**, 165, (1998)

[59] Järvinen, A. *et al. Phys. Scr.* **T145**, 014013, (2011)

[60] Cennachi, G. & Taroni, A. *JET Report JET-IR*, (88) 03, (1988)

[61] Lauro-Taroni, L. *et al. Proc. 21st EPS cond. on Controlled Fusion and Plasma Physics (Montpellier, France)*, p 102, (1994)

[62] Dux, R. *et al. Nucl. Fusion* **51**, 119501, (2011)

[63] Kallenbach, A. *et al. Nucl. Fusion* **51**, 094012, (2011)

[64] Giroud, C. *et al. Proceedings of the 23rd IAEA Fusion Energy Conference, 11 – 16 Oct. Korea*, EXC/P3-02, (2010)

[65] Maddison, G. *et al. Nucl. Fusion Let.* **51**, 042001, (2011)

[66] Tskhakaya, D. *et al. Jour. Nucl. Mater.* **415**, S860 – S864, (2011)

[67] Eich, T. *et al. Plasma Phys. Control. Fusion* **49**, 573 – 604, (2007)

[68] Kallenbach, A. *et al. Plasma Phys. Control. Fusion* **46**, 431 – 446, (2004)

[69] Gulejová, B. *SOLPS Modelling of ELMing H-mode*, PhD Thesis, École Polytechnique Fédérale de Lausanne, (2010)

[70] Moulton, D. *et al. Jour. Nucl. Mater.* **415**, S509 – S512, (2011)

[71] Roth, J. *et al. Nucl. Fusion* **44**, L21 – L25, (2004)

[72] Davis, J. W. & Haasz, A. A. *Jour. Nucl. Mater.* **255**, 214 – 221, (1998)

[73] Eckstein, W. *et al. Sputtering data.*, MPI-Garching, (1993)

[74] Moulton, D. *Numerical Modelling of H-mode Plasmas on JET*, PhD Thesis, Imperial College London, (2011)

[75] Scannell, R. *et al. Rev. Sci. Intsrum.* **82**, 053501, (2011)

[76] Simonini, R. *et al. Contrib. Plasma Phys.* **34**, 368–73, (1994)

[77] Eich, T. *et al. Jour. Nucl. Mater.*, **363 – 365**, 989 – 993, (2007)

[78] Eich, T. *et al. Phys. Rev. Lett.* **107**, 215001, (2011)

[79] Kallenbach, A. *et al. Nucl. Fusion* **48**, 085008, (2008)

[80] Wiesen, S. *et al.* JINTRAC-JET modelling suite *JET ITC-Report*, http://www.eirene.de/JINTRAC_Report_2008.pdf, (2008)

[81] Wiesen, S. *et al. Plasma Phys. Control. Fusion* **53**, 124039, (2011)

[82] Herrmann, A. *et al. Jour. Nucl. Mater.* **313 – 316**, 759 – 767, (2003)

[83] Tskhakaya, D. *et al. Contrib. Plasma Phys.* **48**, 89 – 93, (2008)

[84] Eckstein, W. *Jour. Nucl. Mater.* **248**, 1 – 8, (1997)

[85] Thoma, A. *et al. Plasma Phys. Control. Fusion* **39**, 1487, (1997)

[86] Dux, R. *et al. Jour. Nucl. Mater.* **390 – 391**, 858 – 863, (2009)

[87] Järvinen, A. *et al. Proceedings of the 38th EPS Conference on Plasma Physics*, **P2.067**, (2011)

[88] Neuhauser, J. *et al. Nucl. Fusion* **24**, 39, (1984)

[89] Havlickova, E. *et al. Plasma Phys. Control. Fusion* **54**, 045002, (2012)